UNIVERSITY OF CRETE

SCHOOL OF SCIENCE & ENGINEERING

GRADUATE PROGRAM
"APPLIED AND COMPUTATIONAL MATHEMATICS"

DEPARTMENT OF MATHEMATICS AND
APPLIED MATHEMATICS

Coherent imaging in clutter

Author:
Almpion Ratsakou

Supervisor:
Chrysoula Tsogka

Herakleion
December 14, 2016

Abstract

This thesis concerns the problem of detecting and imaging reflectors in complex scattering media. These are media with small scale inhomogeneities that are not known and cannot be estimated in detail. We usually refer to them as clutter and model them as a random process. Imaging means that we are primarily interested in reconstructing the shape of the reflector and not its actual physical properties. Our data is the array response matrix collected by sending short pulses from each array element and then recording the medium response at the array receivers. The challenge when imaging in clutter is that the array data are noisy, *i.e.*, the echoes from the reflectors that we wish to image are immersed in the multiple reflections of the waves by the medium inhomogeneities.

Coherent interferometry (CINT) is a methodology that has been developed for imaging in such media. The main idea in CINT is to image by back-propagating cross correlations of the data over appropriate space-frequency windows. The size of the windows basically determines the area over which the data are coherent. It depends on the medium heterogeneities and the distance that the waves have traveled in the multiple scattering environment.

Here we rely on a windowed beamformer energy functional that has been shown to be equivalent to CINT for the appropriate choice of window functions. This is a quadratic imaging function that involves only time gating and time delaying signals in emission and in reception. In this form, coherent interferometric imaging can be implemented efficiently both in hardware and software, with a computational cost comparable to the usual beamforming and migration imaging methods.

Moreover, we consider different type of window functions that can be interpreted as filters that enhance the coherent part of the data prior to imaging. This leads to imaging results with improved signal to noise ratio.

Acknowledgments

I would firstly like to thank my advisor, Prof. Chrysoula Tsogka for guiding and supporting me throughout this thesis. She consistently allowed this paper to be my own work, but steered me in the right direction whenever she thought I needed it. She have set an example of excellence as a researcher, mentor and role model.

Besides my advisor, I would like to thank the rest of my thesis committee Prof. Michael Taroudakis and Prof. George Makrakis for their insightful comments.

Last but not least, I would like to thank my family for supporting me throughout all these years.

A.R.

Contents

List of Figures

1 Introduction

This thesis concerns imaging, a research area that belongs in the field of inverse problems. Inverse problems are in general ill-posed, which means that they do not admit a unique solution. To regularize the problem one can add some a-priori information about the unknown properties of the object to be imaged. One such type of information could be that we seek to find small inhomogeneities that have significantly different properties from those of the surrounding medium. In medical imaging those small inhomogeneities may represent small tumors at an early stage.

Ultrasound is used with a great success in the diagnosis of abnormalities in soft tissue structures in the human body. It is non-invasive and cheap. In certain applications such as fetal imaging, it is the only modality considered safe. Ultrasound propagates fast and can be processed fast enough to enable imaging of moving organs as well, such as the heart. It has also been proven that ultrasound is a very useful tool for locating tumors. Cross-sectional images are made in real time with the B-mode scan technique by current scanners. A high image quality is obtained by employing linear and phased array transducers, and by post-processing the envelope detected signal from the transducer. But the ultrasound image still lacks contrast and resolution compared to x-ray and NMR (nuclear magnetic resonance) images. In imaging *resolution* is defined as the minimum distance by which two point objects have to be separated in order to be distinguishable from each other.

Although several numerical techniques have been theoretically developed for getting images with better resolution and signal to noise ratio, they are not always adopted in commercial medical equipment for several reasons. Robustness and easiness in hardware/software implementation is always an issue. Such a technique is coherent interferometric imaging. We will refer to this method as CINT. Coherent interferometric imaging is based on the propagation of the local space-time cross correlations of array data and was introduced in order to improve the performance of back-propagation or beamforming when imaging is carried out in background medium with unknown small scale inhomogeneities [13, 14, 10]. This method has been shown to be effective and is well founded theoretically. However, the CINT functional is computational expensive and therefore difficult to use in practice. A windowed beamformer energy function has been shown to be equivalent to CINT and is expected to have a much lower computational cost [9]. In this thesis we will explore this functional and asses its performance with extensive numerical simulations.

Specifically we consider an active array imaging problem that consists in detecting the presence and determining the location of small reflectors by sending probing signals from one or more sources at the array and recording the scattered echoes. A typical setup is shown in Figure 1.1, where the reflectors are assumed to be in a bounded domain $\mathcal{D}$.

The transmitter located at $\vec{\mathbf{x}}_s$ emits a pulse $f(t)$, whose Fourier transform $\widehat{f}(\omega)$ is supported in the frequency interval centered at ω_0 with a bandwidth B. Assuming a point source behavior, this creates a spherical wave that propagates in the medium and interacts with the reflectors to be imaged. The backscattered field $P(\vec{\mathbf{x}}_s, \vec{\mathbf{x}}_r, t)$ is recorded at all receiver locations $\vec{\mathbf{x}}_r$, for $r = 1, \ldots, N_r$, over some time window $t \in [t_0, T]$. By repeating the same process for all transmitter locations $\vec{\mathbf{x}}_s$, $s = 1, \ldots, N$ we collect the array response matrix $P(\vec{\mathbf{x}}_s, \vec{\mathbf{x}}_r, t),\ s = 1, \ldots, N_s,\ r = 1, \ldots, N_r$. We refer to $P(\vec{\mathbf{x}}_s, \vec{\mathbf{x}}_r, t)$ as the time traces, as in the context of geophysical applications [7].

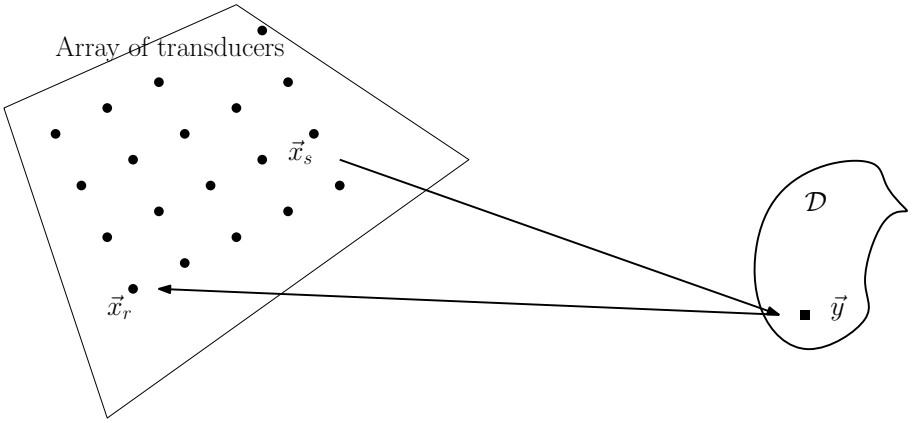

Figure 1.1: Schematic for imaging distributed reflectors in region D.

The imaging problem consists in estimating the support of the reflectors in the domain $\mathcal{D}$. This is an easier problem and often can be addressed as a first step of the full inverse problem in which we seek to determine not only the size and shape but also the actual physical properties of the reflectors.

We illustrate in Figure 1.2 snapshots of the solution of the wave equation during the data acquisition process. In a first step as shown on the left the spherical wave originating from the source propagates into the medium. In this example the background medium is homogeneous and therefore the wave propagates freely until it encounters the scatterer. On the right panel in Figure 1.2 we see a snapshot of the solution at a later time where the direct (ballistic) wave has left the computational domain and the echoes due to three small reflectors are visible. These are the echoes that are recorded on the array and will be used as data to solve the imaging problem.

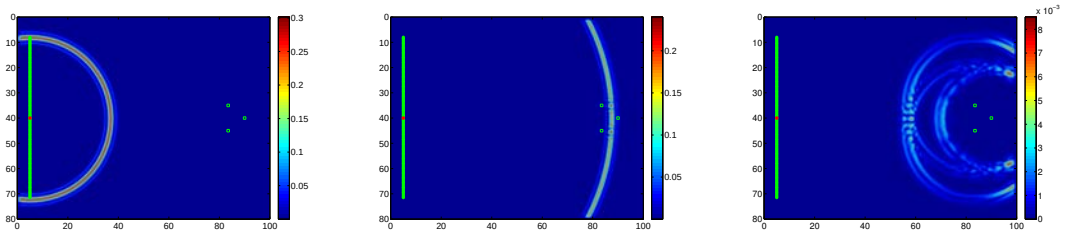

Figure 1.2: Snapshots of the absolute value of the pressure field in the computational domain. From left to right: a pulse is send from the central array element, the incident wave propagates in the medium and when it leaves the computational domain (absorbed by the PML) the echoes from the scatterers are shown (right plot). The scattered echoes propagate back towards the array and are recorded at all array elements.

To be able to simulate the human soft tissue we will use a medium whose propagation sound speed is not constant but has fluctuations on a certain scale. These sound speed fluctuations will produce their own echoes and this will impede the imaging process. Although the strength of the fluctuations is small their effect on the wave accumulates and becomes order one over long propagation distances. Since

the medium inhomogeneities are unknown and cannot be estimated in detail we model them as a random process. The challenge in imaging is to produce reliable statistically stable images of the reflectors in such media. Statistical stability means that the image is independent of the particular realization of the background fluctuations considered. CINT and the windowed beamformer energy (WBE) functional are statistical stable imaging methods as shown in [9, 10].

This thesis is organized as follows: In Section 2 we formulate the array imaging problem and in Section 3 the numerical setup is described. In Section 4 we review the simplest form of imaging with Kirchhoff migration and discuss its limitations when imaging in clutter. We consider coherent interferometric imaging in Section 5 and we illustrate with numerical results the statistical stability of the method, as well as the role of the smoothing parameters. In Section 6 a different approach to array imaging using a windowed energy beamfomer (WBE) is presented. The connection between WBE and CINT is described in Section 6.2. The equivalence of the two methods is shown through some numerical results. In Section 6.3 we present the algorithm for WBE imaging. The performance of WBE is compared to that of CINT in Section 6.4 using different parameters' values for the imaging methods. In Section 7 we address the multiple scattering problem in strong cluttered media. We introduce in Section 7.2 a single scattering filter applied in WBE in a simpler form than the one proposed in [2, 3]. In Section 7.3 the implementation of the filter is discussed and in Section 7.4 we test the efficiency of the filter when imaging in strong cluttered media. We end with a summary in Section 8.

2 The array imaging problem

In this section we want to describe the array imaging problem in detail. We begin with the basics of the wave propagation problem. Then we derive a model that describes the relation between the reflectivity and the recorded pressure field using the Born approximation and finally the Kirchhoff Migration imaging function is introduced.

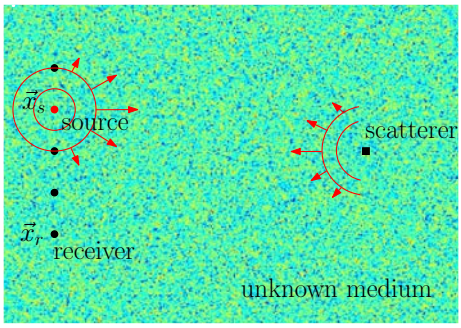

Figure 2.1: The array imaging problem. A source located at $\vec{\mathbf{x}}_s$ sends a probing pulse and the echoes are recorded at all array elements $\vec{\mathbf{x}}_r$, $r = 1, 2, \ldots, N$.

2.1 The wave equation

In this section we present a few basic facts about the wave equation and wave propagation. The propagation of sound waves is modeled by a first order system of equations driven by a force $\vec{\mathcal{F}}(t, \vec{\mathbf{x}})$ exerted by an acoustic source. The resulting pressure field $p(t, \vec{\mathbf{x}})$ and the particle velocity $\vec{\mathbf{v}}(t, \vec{\mathbf{x}})$ satisfy the equations of conservation of momentum

$$\varrho(\vec{\mathbf{x}}) \frac{\partial \vec{\mathbf{v}}(t, \vec{\mathbf{x}})}{\partial t} + \nabla p(t, \vec{\mathbf{x}}) = \vec{\mathcal{F}}(t, \vec{\mathbf{x}}), \tag{2.1}$$

and the conservation of mass

$$\frac{\partial p(t, \vec{\mathbf{x}})}{\partial t} + K(\vec{\mathbf{x}}) \nabla \cdot \vec{\mathbf{v}}(t, \vec{\mathbf{x}}) = 0, \tag{2.2}$$

for $t > 0$ and $\vec{\mathbf{x}} \in \mathbb{R}^n$. Where $K(\vec{\mathbf{x}})$ is the bulk modulus and $\varrho(\vec{\mathbf{x}})$ is the mass density of the medium. The force $\vec{\mathcal{F}}(t, \vec{\mathbf{x}})$ is supported at $t > 0$ and the medium for $t \leq 0$ is in its equilibrium state,

$$p(t, \vec{\mathbf{x}}) = 0, \qquad \vec{\mathbf{v}}(t, \vec{\mathbf{x}}) = \mathbf{0}, \qquad t \leq 0.$$

When taking the time derivative in (2.2) and substituting (2.1), the first order system (2.1-2.2) reduces to a second order equation for the pressure field. We obtain that $p(t, \vec{\mathbf{x}})$ satisfies

$$\frac{\varrho(\vec{\mathbf{x}})}{K(\vec{\mathbf{x}})} \frac{\partial^2 p(t, \vec{\mathbf{x}})}{\partial t^2} - \varrho(\vec{\mathbf{x}}) \nabla \cdot \left[\frac{\nabla p(t, \vec{\mathbf{x}})}{\varrho(\vec{\mathbf{x}})} \right] = -\varrho(\vec{\mathbf{x}}) \nabla \cdot \left[\frac{\vec{\mathcal{F}}(t, \vec{\mathbf{x}})}{\varrho(\vec{\mathbf{x}})} \right], \quad t > 0, \quad \vec{\mathbf{x}} \in \mathbb{R}^n, \tag{2.3}$$

with initial condition

$$p(0,\vec{\mathbf{x}}) = \frac{\partial p(0,\vec{\mathbf{x}})}{\partial t} = 0. \tag{2.4}$$

Under the assumption that the density ϱ is constant from (2.4) we have the canonical form of the wave equation

$$\frac{1}{c^2(\vec{\mathbf{x}})}\frac{\partial^2 p(t,\vec{\mathbf{x}})}{\partial t^2} - \Delta p(t,\vec{\mathbf{x}}) = F(t,\vec{\mathbf{x}}), \quad \vec{\mathbf{x}} \in \mathbb{R}^n, \quad t > 0, \tag{2.5}$$

with wave speed

$$c(\vec{\mathbf{x}}) = \sqrt{\frac{K(\vec{\mathbf{x}})}{\varrho}},$$

and source density

$$F(t,\vec{\mathbf{x}}) = -\nabla \cdot \vec{\mathcal{F}}(t,\vec{\mathbf{x}}).$$

Let us consider a linear array $\mathcal{A}$ which has $N \geq 1$ elements. We assume here that these elements will act as transmitters and receivers. That means that the sources (transmitters) and the receivers are collocated, an assumption made for simplicity which is not necessary in practice. The sources may emit simultaneously, but we assume in the following that the excitation is emitted from one source at a time. Let us further suppose that the sources are small and can be assumed to have a point-like support at location $\vec{\mathbf{x}}_s \in \mathcal{A}$, for $s = 1, \ldots, N$.

$$F(t,\mathbf{x}_s) = f(t)\delta(\vec{\mathbf{x}} - \vec{\mathbf{x}}_s). \tag{2.6}$$

The receivers are also point-like transducers located at $\vec{\mathbf{x}}_r \in \mathcal{A}$, for $r = 1, \ldots, N$.

What we seek to reconstruct in imaging is the reflectivity of the medium, denoted ρ, which is a perturbation of the medium velocity resulting in the following change

$$\frac{1}{c^2(\vec{\mathbf{x}})} \rightsquigarrow \frac{1}{c^2(\vec{\mathbf{x}})} + \frac{\rho(\vec{\mathbf{x}})}{c_0^2}.$$

Here $c(\vec{\mathbf{x}})$ is the assumed known wave speed in the background medium which hosts the perturbation $\rho(\vec{\mathbf{x}})$ that we wish to estimate.

To emphasize the dependence of the waves to the source location, we denote the pressure field due to source (2.6) by $p(t,\vec{\mathbf{x}};\vec{\mathbf{x}}_s)$. It satisfies

$$\frac{1}{c^2(\vec{\mathbf{x}})}\frac{\partial^2 p(t,\vec{\mathbf{x}};\vec{\mathbf{x}}_s)}{\partial t^2} - \Delta_{\vec{\mathbf{x}}} p(t,\vec{\mathbf{x}};\vec{\mathbf{x}}_s) = -\frac{\rho(\vec{\mathbf{x}})}{c_0^2}\frac{\partial^2 p(t,\vec{\mathbf{x}};\vec{\mathbf{x}}_s)}{\partial t^2} + f(t)\delta(\vec{\mathbf{x}} - \vec{\mathbf{x}}_s), \quad t > 0, \tag{2.7}$$

with initial condition

$$p(0,\vec{\mathbf{x}};\vec{\mathbf{x}}_s) = \frac{\partial}{\partial t} p(0,\vec{\mathbf{x}};\vec{\mathbf{x}}_s) = 0.$$

Let us further assume that the background medium contains some small scale inhomogeneities. Due to band-limited array data it is impossible to recover all these fluctuations in detail as part of the imaging process. This motivates us to separate the wave speed in two parts. The first part is the clutter or micro-structure which is the unknown part of $c(\vec{\mathbf{x}})$ which we will not recover in imaging and the second part is the perturbation which can be recovered in imaging, lets call this the reflectivity. We can write now, our model for the velocity in the medium,

$$\frac{1}{c^2(\vec{\mathbf{x}})} = \frac{1}{c_0^2}[1 + \mu(\vec{\mathbf{x}})] + \frac{\rho(\vec{\mathbf{x}})}{c_0^2} \tag{2.8}$$

where c_0 is a reference speed, $\rho(\vec{\mathbf{x}})$ the reflectivity and $\mu(\vec{\mathbf{x}})$ the perturbation that represents the clutter.

(a) *Homogeneous medium.*

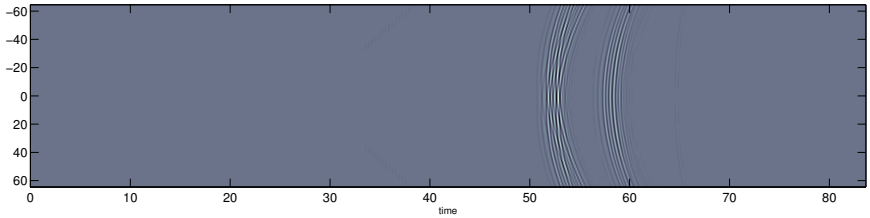

(b) *Inhomogeneous medium.*

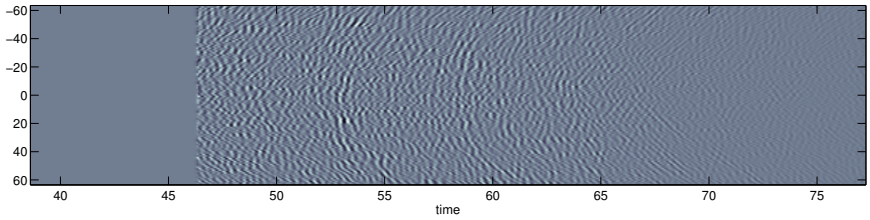

Figure 2.2: Traces received in (a) homogeneous and (b) inhomogeneous background, when signal $f(t)$ is sent from the central array element. The vertical axis is the receiver location, scaled by λ_0. The horizontal axis is time in μsec.

A very important factor in imaging is the scaling. We use it to classify different imaging regimes based on the relation between the length scales of the problem. The reference scale we usually use is the central wavelength λ_0 which is defined by

$$\lambda_0 = c_0/f_0$$

where c_0 is the reference wave speed and f_0 the central frequency of the probing wave send by the source.

We define as L the *range* scale which is the typical distance from the array to the imaging region. We call also range the main direction of propagation of the waves. In this thesis we are interesed in *far-field* imaging, that means $L \gg \lambda_0$. The direction orthogonal to the range direction is called *cross-range*. This is the direction in which the array lies on. In two dimensions the array is linear while in three dimensions the arrays are usually planar. As we will see, the *resolution* in imaging is highly dependent on the range and the array size. The size of the array in the cross-range direction is called also *aperture size* and we denote it by a. We say that the arrays are small when $a \ll L$, and large when $a \geq L$. The imaging process can be done with *full aperture* or *partial aperture*. In the first case the imaging region is surrounded by the array while in the second one the array lies on one side of the imaging window $\mathcal{I}_{\mathrm{W}}$. The imaging window is the region of interest that contains the reflectors to be imaged. Typically in imaging we discretize the $\mathcal{I}_{\mathrm{W}}$ and create an image by associating a value of an imaging functional to each point of the $\mathcal{I}_{\mathrm{W}}$.

In random media we need a reference scale to describe the inhomogeneities. This scale will be the scale at which the medium fluctuates, so called *the correlation length* and denoted C_l. It is obvious that the inhomogeneities are not all of the same size,

so for complex media we can have different length scales C_l. Here we will consider rather simple media that can be described by one length scale C_l. We suppose moreover that the medium varies on the same scale in all directions. This is an *isotropic* medium.

Another important quantity for imaging is the *bandwidth* B. When the central frequency f_0 is of the same order as the bandwidth B, we say that we have a *broadband* signal $f(t)$.

2.2 The Born approximation

At this point we want to derive an explicit relation between the source $F(t, \vec{\mathbf{x}})$ and the wave field $p(t, \vec{\mathbf{x}})$. To do so, we need to invert the wave operator in (2.5), which we denote by $\mathbb{T}$. It is a linear operator defined on the vector space of twice continuously differentiable functions of t and $\vec{\mathbf{x}}$. Equation (2.5) becomes $\mathbb{T}p = F$, and it has a unique solution

$$p = \mathbb{T}^{-1}F. \tag{2.9}$$

The inverse of the operator is an integral operator with kernel given by the causal Green's function

$$G_0(t, \vec{\mathbf{x}}, \vec{\mathbf{y}}) = \frac{1}{4\pi|\vec{\mathbf{x}} - \vec{\mathbf{y}}|}\delta\left(t - \frac{|\vec{\mathbf{x}} - \vec{\mathbf{y}}|}{c_0}\right), \quad t > 0 \tag{2.10}$$

under the assumption that the wave speed is constant in the medium $c(\vec{\mathbf{x}}) = c_0$. The equation (2.9) has the explicit form

$$p(t, \vec{\mathbf{x}}) = \int_0^t \mathrm{d}s \int_{\mathbb{R}^n} \mathrm{d}\vec{\mathbf{y}}\, F(s, \vec{\mathbf{y}})G(t - s, \vec{\mathbf{y}}, \vec{\mathbf{x}}), \tag{2.11}$$

known as Duhamel's principle. The causal Green's function satisfies

$$\begin{aligned} \frac{1}{c^2(\vec{\mathbf{x}})}\frac{\partial^2 G(t, \vec{\mathbf{x}}, \vec{\mathbf{y}})}{\partial t^2} - \Delta_{\vec{\mathbf{x}}} G(t, \vec{\mathbf{x}}, \vec{\mathbf{y}}) &= \delta(\vec{\mathbf{x}} - \vec{\mathbf{y}})\delta(t), \quad \vec{\mathbf{x}}, \vec{\mathbf{y}} \in \mathbb{R}^n, \quad t > 0, \\ G(t, \vec{\mathbf{x}}, \vec{\mathbf{y}}) &= 0, \quad t < 0, \end{aligned}$$

where $\Delta_{\vec{\mathbf{x}}}$ is the Laplacian operator in the variable $\vec{\mathbf{x}}$, and δ is the Dirac distribution. Since both the Green's function and the source are supported at positive time we have

$$\int_0^t \mathrm{d}s\, F(s, \vec{\mathbf{y}})G(t - s), \vec{\mathbf{x}}, \vec{\mathbf{y}}) = \int_{-\infty}^{+\infty} \mathrm{d}s\, F(s, \vec{\mathbf{y}})G(t - s, \vec{\mathbf{y}}, \vec{\mathbf{x}}) = F(t, \vec{\mathbf{y}}) *_t G(t, \vec{\mathbf{x}}, \vec{\mathbf{y}})$$

so we can rewrite the equation (2.11) as a time convolution

$$p(t, \vec{\mathbf{x}}) = \int_{\mathbb{R}^n} \mathrm{d}\vec{\mathbf{y}}\, F(t, \vec{\mathbf{y}}) *_t G(t, \vec{\mathbf{y}}, \vec{\mathbf{x}}). \tag{2.12}$$

Often it is not easy to deal with convolutions. A way to avoid time convolutions is to work in the frequency domain using the Fourier transform. The Fourier transform of the pressure filed is defined as

$$\widehat{p}(\omega, \vec{\mathbf{x}}) = \int_{-\infty}^{+\infty} \mathrm{d}t\, p(t, \vec{\mathbf{x}})e^{i\omega t},$$

and the inverse Fourier transform is

$$p(t,\vec{\mathbf{x}}) = \int_{-\infty}^{+\infty} \frac{\mathrm{d}\omega}{2\pi} \widehat{p}(\omega,\vec{\mathbf{x}}) e^{-i\omega t}.$$

The advantage of working in the Fourier domain is that time convolutions become products and the equation (2.12) simplifies to

$$\widehat{p}(\omega,\vec{\mathbf{x}}) = \int_{R^n} \mathrm{d}\vec{\mathbf{y}}\ \widehat{F}(\omega,\vec{\mathbf{y}}) \widehat{G}(\omega,\vec{\mathbf{y}},\vec{\mathbf{x}}),$$

where $\widehat{G}(\omega,\vec{\mathbf{y}},\vec{\mathbf{x}})$ is the Fourier transform of the Green's function,

$$\widehat{G}(\omega,\vec{\mathbf{y}},\vec{\mathbf{x}}) = \int_{-\infty}^{+\infty} \mathrm{d}t\ G(t,\vec{\mathbf{y}},\vec{\mathbf{x}}) e^{i\omega t},$$

which is the solution of the Helmholtz equation

$$\left(\Delta_{\vec{\mathbf{x}}} + \frac{\omega^2}{c^2(\vec{\mathbf{x}})}\right) \widehat{G}(\omega,\vec{\mathbf{x}},\vec{\mathbf{y}}) = -\delta(\vec{\mathbf{x}}-\vec{\mathbf{y}}), \tag{2.13}$$

with the Sommerfeld radiation condition at infinity (assuming that the medium is homogeneous with velocity c_0 outside a compact region)

$$\lim_{|\vec{\mathbf{x}}-\vec{\mathbf{y}}|\to\infty} |\vec{\mathbf{x}}-\vec{\mathbf{y}}|^{(n-1)/2} \left(\frac{(\vec{\mathbf{x}}-\vec{\mathbf{y}})}{|\vec{\mathbf{x}}-\vec{\mathbf{y}}|}\cdot\nabla_{\vec{\mathbf{x}}} - i\frac{\omega}{c_0}\right) \widehat{G}(\omega,\vec{\mathbf{x}},\vec{\mathbf{y}}) = 0. \tag{2.14}$$

The variable ω here is the angular frequency and it is related to the frequency f by

$$\omega = 2\pi f.$$

Often we refer to ω as frequency. We also relate the angular frequency ω to the wavelength $\lambda = c_0/f$ using a reference wave speed c_0,

$$k = \frac{\omega}{c_0} = \frac{2\pi}{\lambda},$$

where k is defined as the wavenumber.

In the analysis of imaging functions we will need to switch the role of sources and receivers. The reciprocity of the Green's function will allow us to do so. The reciprocity relation

$$\widehat{G}(\omega,\vec{\mathbf{x}},\vec{\mathbf{y}}) = \widehat{G}(\omega,\vec{\mathbf{y}},\vec{\mathbf{x}}) \tag{2.15}$$

expresses the fact that the wave field recorded at $\vec{\mathbf{x}}$ due to a point source $\vec{\mathbf{y}}$ is the same as the wave field recorded at point $\vec{\mathbf{y}}$, due to a point source $\vec{\mathbf{x}}$.

Now we can rewrite the pressure field equation (2.7) using the Green's function

$$p(t,\vec{\mathbf{x}},\vec{\mathbf{x}}_s) = f(t) \star_t G(t,\vec{\mathbf{x}},\vec{\mathbf{x}}_s) - \int_{\mathcal{I}_{\mathrm{W}}} \mathrm{d}\vec{\mathbf{y}}\ \frac{\rho(\vec{\mathbf{y}})}{c_0^2} \frac{\partial^2 p(t,\vec{\mathbf{y}},\vec{\mathbf{x}}_s)}{\partial t^2} \star_t G(t,\vec{\mathbf{x}},\vec{\mathbf{y}}). \tag{2.16}$$

In this equation, $\vec{\mathbf{x}}$ stands for any point and we want now to evaluate this at $\vec{\mathbf{x}} = \vec{\mathbf{x}}_r$, the receiver locations for $r = 1,\ldots,N_r$. From the above equation, the term $f(t) \star_t G(t,\vec{\mathbf{x}},\vec{\mathbf{x}}_s)$ is the direct wave that does not interact with the reflectivity and we can remove it by windowing. This is possible assuming that the reflectors

to imaged are not very close to the array. As wee can see, the dependence of the pressure field $p(t, \vec{\mathbf{x}}, \vec{\mathbf{x}}_r)$ on the reflectivity ρ is nonlinear. To simplify the problem, the following linearization, called the Born approximation of the pressure field, is widely used in imaging.

We will begin with the Fourier transform of (2.16),

$$\widehat{p}^{sc}(\omega, \vec{\mathbf{x}}, \vec{\mathbf{x}}_s) = k^2 \int_{\mathcal{I}_{\mathrm{W}}} \mathrm{d}\vec{\mathbf{y}}\ \rho(\vec{\mathbf{y}}) \left[\widehat{p}^{inc}(\omega, \vec{\mathbf{y}}, \vec{\mathbf{x}}_s) + \widehat{p}^{sc}(\omega, \vec{\mathbf{y}}, \vec{\mathbf{x}}_s)\right] \widehat{G}(\omega, \vec{\mathbf{x}}, \vec{\mathbf{y}}), \qquad (2.17)$$

where we have split the pressure field in two parts. The first part

$$\widehat{p}^{inc}(\omega, \vec{\mathbf{y}}, \vec{\mathbf{x}}_s) = \widehat{f}(\omega)\widehat{G}(\omega, \vec{\mathbf{x}}, \vec{\mathbf{x}}_s)$$

is the incident wave which has not interacted with ρ and the second part

$$\widehat{p}^{sc}(\omega, \vec{\mathbf{y}}, \vec{\mathbf{x}}) = \widehat{p}(\omega, \vec{\mathbf{x}}, \vec{\mathbf{y}}) - \widehat{p}^{inc}(\omega, \vec{\mathbf{x}}, \vec{\mathbf{y}})$$

is the scattered field. Substituting now $\widehat{p}^{sc}$ in the right hand side of (2.17) we obtain the Born series. The Born approximation is just the first term of the series

$$\begin{aligned} \widehat{p}^{Born}(\omega, \vec{\mathbf{x}}, \vec{\mathbf{x}}_s) &= k^2 \int_{\mathcal{I}_{\mathrm{W}}} \mathrm{d}\vec{\mathbf{y}}\ \rho(\vec{\mathbf{y}})\widehat{p}^{inc}(\omega, \vec{\mathbf{y}}, \vec{\mathbf{x}}_s)\widehat{G}(\omega, \vec{\mathbf{x}}, \vec{\mathbf{y}}) \\ &= k^2 \widehat{f}(\omega) \int_{\mathcal{I}_{\mathrm{W}}} \mathrm{d}\vec{\mathbf{y}}\ \rho(\vec{\mathbf{y}})\widehat{G}(\omega, \vec{\mathbf{x}}_s, \vec{\mathbf{y}})\widehat{G}(\omega, \vec{\mathbf{y}}, \vec{\mathbf{x}}). \qquad (2.18) \end{aligned}$$

In homogeneous media a sufficient condition, for the Born approximation to hold, is that either the support of ρ is very small or ρ itself is small. We define the mean square reflectivity as

$$\left[\langle \rho^2 \rangle\right]^{1/2} = \frac{3}{4\pi R^3} \int_{\mathcal{B}_R(\vec{\mathbf{y}}^\star)} \mathrm{d}\vec{\mathbf{y}} \rho^2(\vec{\mathbf{y}}),$$

where R is the radius of the ball $\mathcal{B}_R(\vec{\mathbf{y}}^\star) \subset \mathbb{R}^3$ centered at $\vec{\mathbf{y}}^\star$, which contains the support of ρ. The condition is

$$\left(\frac{R}{\lambda}\right)^2 \left[\langle \rho^2 \rangle\right]^{1/2} \ll 1, \qquad (2.19)$$

where R is small with respect to the wavelength λ and/or the mean square reflectivity is small. For a detailed analysis we refer to [23].

2.3 Pulse model and propagation

We model the pulse $f(t)$ as a base-band pulse $f_B(t)$ modulated by a harmonic signal at central frequency $f_0 = \frac{\omega_0}{2\pi}$,

$$f(t) = cos(\omega_0 t) f_B(t).$$

In the frequency domain we have

$$\begin{aligned} \widehat{f}(\omega) &= \int_{-\infty}^{+\infty} \mathrm{d}\omega\ f(t) e^{i\omega t} \\ &= \frac{1}{2}\left[\widehat{f}_B(\omega - \omega_0) + \widehat{f}_B(\omega + \omega_0)\right]. \end{aligned}$$

Because the Fourier transform $\widehat{f_B}(\omega)$ is supported at $\omega \in [-\pi B, \pi B]$, the signal $f_B(t)$ is called base-band. Then, the frequencies $f = \omega/2\pi$ in the support of $\widehat{f}(\omega)$ lie in the interval centered at f_0, of bandwidth B

$$f \in [f_0 - B/2, f_0 + B/2] \cup [-f_0 - B/2, -f_0 + B/2]\,.$$

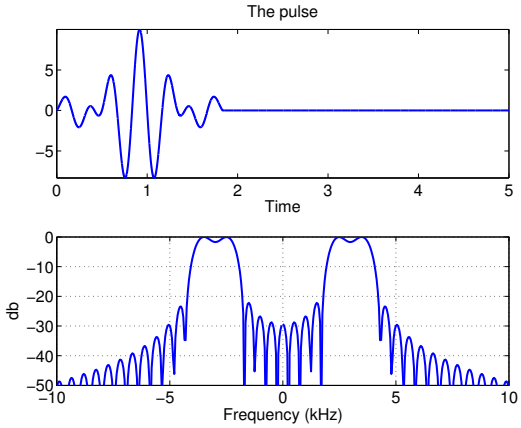

Figure 2.3: The pulse in the time (top) and in the frequency (bottom) domain.

The convolution of the pulse with the Green's function in smooth media is given by

$$\begin{aligned} f(t) \star_t G(t, \vec{\mathbf{x}}, \vec{\mathbf{y}}) &\approx \alpha(\vec{\mathbf{x}}, \vec{\mathbf{y}}) \int_{-\infty}^{+\infty} \frac{\mathrm{d}\omega}{2\pi} \widehat{f}(\omega) e^{i\omega\tau(\vec{\mathbf{x}},\vec{\mathbf{y}}) - i\omega t} \\ &= \alpha(\vec{\mathbf{x}}, \vec{\mathbf{y}}) f\left[t - \tau(\vec{\mathbf{x}}, \vec{\mathbf{y}})\right]. \end{aligned}$$

The time delays are the travel times $\tau(\vec{\mathbf{x}}, \vec{\mathbf{y}})$. The pulse retains its shape as it travels through the medium, but its strength diminishes because the *amplitude* $\alpha(\vec{\mathbf{x}}, \vec{\mathbf{y}})$ decays due to geometrical spreading of the wave.

2.4 The forward map

The Born data model in the frequency domain is

$$\widehat{P}(\omega, \vec{\mathbf{x}}_r, \vec{\mathbf{x}}_s) \approx k^2 \widehat{f}(\omega) \int_{\mathcal{I}_{\mathrm{W}}} \mathrm{d}\vec{\mathbf{y}}\ \rho(\vec{\mathbf{y}}) \widehat{G}(\omega, \vec{\mathbf{x}}_r, \vec{\mathbf{y}}) \widehat{G}(\omega, \vec{\mathbf{y}}, \vec{\mathbf{x}}_s).$$

The forward map $\mathcal{M} : L^2(\mathcal{I}_{\mathrm{W}}) \to \mathbb{P}$ takes square integrable reflectivity functions ρ to functions in the data space

$$\mathbb{P} = \left\{ \widehat{P}(\omega, \vec{\mathbf{x}}_r, \vec{\mathbf{x}}_s) \in \mathbb{C},\ \sum_{r=1}^{N_r} \sum_{s=1}^{N_s} \int_{|\omega \pm \omega_0| \leq \pi B} \mathrm{d}\omega |\widehat{P}(\omega, \vec{\mathbf{x}}_r, \vec{\mathbf{x}}_s)|^2 < \infty \right\}, \tag{2.20}$$

with complex inner product

$$\langle \widehat{P}, \widehat{R} \rangle = \int_{|\omega \pm \omega_0| \leq \pi B} \mathrm{d}\omega \sum_{r=1}^{N_r} \sum_{s=1}^{N_s} \overline{\widehat{P}(\omega, \vec{\mathbf{x}}_r, \vec{\mathbf{x}}_s)} \widehat{R}(\omega, \vec{\mathbf{x}}_r, \vec{\mathbf{x}}_s), \quad \forall \widehat{P}, \widehat{R} \in \mathbb{P},$$

and induced norm

$$||\widehat{P}||_{\mathbb{P}} = \sqrt{\langle \widehat{P}, \widehat{P} \rangle} = \left[\sum_{r=1}^{N_r} \sum_{s=1}^{N_s} \int_{|\omega \pm \omega_0| \leq \pi B} \mathrm{d}\omega \left| \widehat{P}(\omega, \vec{\mathbf{x}}_r, \vec{\mathbf{x}}_s) \right|^2 \right]^{1/2}.$$

Here $\widehat{P}(\omega, \vec{\mathbf{x}}_r, \vec{\mathbf{x}}_s)$ are the Fourier transforms of the time traces, the entries in the array response matrix

$$\mathbb{P}(t) = \{P(t, \vec{\mathbf{x}}_r, \vec{\mathbf{x}}_s)\}, \quad t \in (0, T], \ \vec{\mathbf{x}}_r, \vec{\mathbf{x}}_s \in \mathcal{A}, \ r = 1, \ldots, N_r, \ s = 1, \ldots, N_s.$$

The map itself is given by

$$[\mathcal{M}\rho](\omega, \vec{\mathbf{x}}_r, \vec{\mathbf{x}}_s) = k^2 \widehat{f}(\omega) \int_{\mathcal{I}_{\mathrm{W}}} \mathrm{d}\vec{\mathbf{y}} \ \rho(\vec{\mathbf{y}}) \widehat{G}(\omega, \vec{\mathbf{x}}_r, \vec{\mathbf{y}}) \widehat{G}(\omega, \vec{\mathbf{y}}, \vec{\mathbf{x}}_s) \tag{2.21}$$

which assumes that both the Fourier transform of the pulse $\widehat{f}(\omega)$ and the Green's function are known.

2.5 Imaging with active arrays

In imaging with active arrays the estimation of the unknown reflectivity ρ is computed by a minimizer of

$$\begin{aligned} \mathcal{O}(\rho) &= \|\widehat{P} - \mathcal{M}\rho\|_{\mathbb{P}}^2 \\ &= \int_{|\omega \pm \omega_0| \leq \pi B} \mathrm{d}\omega \sum_{r=1}^{N_r} \sum_{s=1}^{N_s} \left| \widehat{P}(\omega, \vec{\mathbf{x}}_r, \vec{\mathbf{x}}_s) - [\mathcal{M}\rho](\omega, \vec{\mathbf{x}}_r, \vec{\mathbf{x}}_s) \right|^2 \end{aligned}$$

and satisfies the normal equations

$$[\mathcal{M}^\star \mathcal{M}\rho](\vec{\mathbf{y}}^S) = \left[\mathcal{M}^\star \widehat{P}\right](\vec{\mathbf{y}}^S), \quad \forall \vec{\mathbf{y}}^S \in \mathcal{I}_{\mathrm{W}}$$

where the adjoint operator has the explicit expression

$$\left[\mathcal{M}^\star \widehat{P}\right](\vec{\mathbf{y}}^S) = \int_{|\omega \pm \omega_0| \leq \pi B} \mathrm{d}\omega \ k^2 \widehat{f}(\omega) \sum_{r=1}^{N_r} \sum_{s=1}^{N_s} \overline{\widehat{P}(\omega, \vec{\mathbf{x}}_r, \vec{\mathbf{x}}_s)} \widehat{G}(\omega, \vec{\mathbf{y}}^S, \vec{\mathbf{x}}_r) \widehat{G}(\omega, \vec{\mathbf{y}}^S, \vec{\mathbf{x}}_s) \tag{2.22}$$

and

$$\rho(\vec{\mathbf{y}}^S) \sim \left[\mathcal{M}^\star \widehat{P}\right](\vec{\mathbf{y}}^S).$$

The meaning of the symbol $\sim$ here is that large values of the right-side correspond to points in the vicinity of the support of ρ. Thus we may think of $\left[\mathcal{M}^\star \widehat{P}\right](\vec{\mathbf{y}}^S)$ as an imaging function.

Backpropagation or Kirchhoff-Migration (KM) is the exactly this imaging function

$$\mathcal{I}(\vec{\mathbf{y}}^S) = \int_{|\omega \pm \omega_0| \leq \pi B} \frac{\mathrm{d}\omega}{2\pi} \sum_{r=1}^{N_r} \sum_{s=1}^{N_s} \overline{\widehat{P}(\omega, \vec{\mathbf{x}}_r, \vec{\mathbf{x}}_s)} \widehat{G}(\omega, \vec{\mathbf{y}}^S, \vec{\mathbf{x}}_r) \widehat{G}(\omega, \vec{\mathbf{y}}^S, \vec{\mathbf{x}}_s). \tag{2.23}$$

3 Numerical simulations setup

We present in this section the general setup for our numerical simulations. Figure 3.1 shows the two configurations that we will use in our numerical simulations. The dimensions are given in terms of the central wavelength λ_0. We use an array $\mathcal{A}$ of $N_s = N_r = N = 128$ elements at a distance $h = \lambda_0/2$ from each other. The object to be imaged is at range L and at zero cross-range, measured with respect to the center of the array. When the single object is replaced by three reflectors we talk about the center of mass of those three objects. The objects to be imaged are modelled as square scatterers. We will use different reflectivity and different side lengths to make the scatterers weaker or stronger. We will precise the parameters used when we show the numerical results.

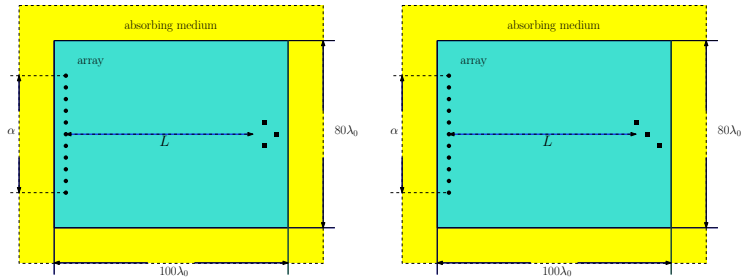

(a) **(b)**

Figure 3.1: The computational setup. The dimensions of the problem are given in terms of the central wavelength λ_0.

A probing pulse is emitted by a source and the echoes are recorded by all the receivers simultaneously. We do not send the pulse simultaneously from all the sources but we probe the medium by a single source at a time. All the sources send the same pulse $f(t)$, which is the time derivative of a *sinc* function with central frequency $f_0 = 3$MHz as used in [3] and bandwidth $B = [2, 4]$MHz (measured at 10dB). With a propagation speed of $c_0 = 3$km/s the central wavelength is $\lambda_0 = 1$mm.

To model the inhomogeneities of the background medium, the index of refraction $n(\vec{\mathbf{x}}) = c_0/c(\vec{\mathbf{x}})$ is assumed to be a statistically homogeneous process so that

$$n^2(\vec{\mathbf{x}}) = 1 + \sigma_0 \mu \left(\frac{\vec{\mathbf{x}}}{C_l} \right),$$

where C_l is the correlation length and σ_0 the standard deviation of the fluctuations of $n^2(\vec{\mathbf{x}})$. The fluctuations in the sound speed $c(\vec{\mathbf{x}})$ are modeled using random Fourier series with mean $c_0 = 3$km/s and a Gaussian correlation function. A typical realisation of the fluctuations is shown in Figure 3.2 where the correlation length is $C_l = 0.18\lambda_0$ and the strength of the fluctuations $\sigma_0 = 3\%$.

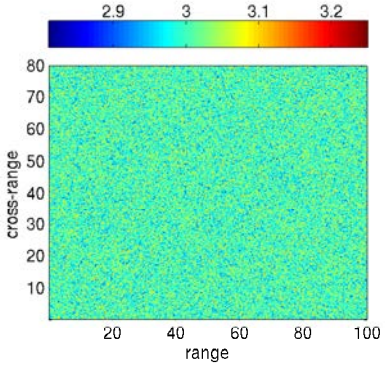

Figure 3.2: A typical realization of the random sound speed $c(\mathbf{x})$. The dimensions are given in terms of the central wavelength λ_0.

To generate the array data we solve the acoustic wave equation, formulated as a first order in time velocity-pressure system, using a mixed finite element method [4, 5]. The propagation medium is considered to be infinite in all directions and in the numerical computations a perfectly matched absorbing layer (PML) [6] surrounds the physical domain as shown in Figure 3.1.

4 Kirchhoff migration imaging

Due to the least square approach we obtained the imaging function (2.23), which assumes that we know the background medium in order to compute the reflectivity. Thus if we replace the Green's function $\widehat{G}$ in (2.23) by the Green's function $\widehat{G}_0$ which is the Green's function in the synthetic background medium that represent our guess of the true one, the result is the following Kirchhoff migration, also caller reverse time migration functional

$$\begin{aligned}
\mathcal{I}^M(\vec{\mathbf{y}}^S) &= \int_{|\omega\pm\omega_0|\leq\pi B} \frac{\mathrm{d}\omega}{2\pi} \sum_{r=1}^{N_r}\sum_{s=1}^{N_s} \overline{\widehat{P}(\omega,\vec{\mathbf{x}}_r,\vec{\mathbf{x}}_s)}\widehat{G}_0(\omega,\vec{\mathbf{y}}^S,\vec{\mathbf{x}}_r)\widehat{G}_0(\omega,\vec{\mathbf{y}}^S,\vec{\mathbf{x}}_s) \\
&\approx \int_{|\omega\pm\omega_0|\leq\pi B} \frac{\mathrm{d}\omega}{2\pi} \sum_{r=1}^{N_r}\sum_{s=1}^{N_s} \overline{\widehat{P}(\omega,\vec{\mathbf{x}}_r,\vec{\mathbf{x}}_s)}\alpha(\vec{\mathbf{y}}^S,\vec{\mathbf{x}}_r)\alpha(\vec{\mathbf{y}}^S,\vec{\mathbf{x}}_s)e^{i\omega[\tau(\vec{\mathbf{y}}^S,\vec{\mathbf{x}}_r)+\tau(\vec{\mathbf{y}}^S,\vec{\mathbf{x}}_s)]} \\
&= \sum_{r=1}^{N_r}\sum_{s=1}^{N_s} P\left(\tau(\vec{\mathbf{y}}^S,\vec{\mathbf{x}}_r)+\tau(\vec{\mathbf{y}}^S,\vec{\mathbf{x}}_s),\vec{\mathbf{x}}_r,\vec{\mathbf{x}}_s\right)\alpha(\vec{\mathbf{y}}^S,\vec{\mathbf{x}}_r)\alpha(\vec{\mathbf{y}}^S,\vec{\mathbf{x}}_s).
\end{aligned}$$

Here we used as $\widehat{G}_0$ the Green's function in the reference homogeneous medium. Neglecting now the geometrical spreading factors $\alpha(\vec{\mathbf{y}}^S,\vec{\mathbf{x}}_r)$ and $\alpha(\vec{\mathbf{y}}^S,\vec{\mathbf{x}}_s)$ from $\mathcal{I}^M(\vec{\mathbf{y}}^S)$ we obtain a simplified version of KM.

Kirchhoff migration forms an image by propagating numerically, or migrating the entries in $\mathbb{P}(t)$ to $\mathbf{y}^{\mathcal{S}} \in \mathcal{D}$, and then summing over sources and receivers,

$$\mathcal{I}^{\mathbf{KM}}(\mathbf{y}^{\mathcal{S}}) = \sum_{r,s} P\left(\tau(\mathbf{x}_r,\mathbf{y}^{\mathcal{S}})+\tau(\mathbf{x}_s,\mathbf{y}^{\mathcal{S}}),\mathbf{x}_r,\mathbf{x}_s\right).$$

Equivalently, in the frequency domain we have

$$\mathcal{I}^{\mathbf{KM}}(\mathbf{y}^{\mathcal{S}}) = \sum_{r,s}\int_{-\infty}^{+\infty} \mathrm{d}\omega\ \widehat{P}(\mathbf{x}_r,\mathbf{x}_s,\omega)\exp\left\{-i\omega\left[\tau(\mathbf{x}_r,\mathbf{y}^{\mathcal{S}})+\tau(\mathbf{x}_s,\mathbf{y}^{\mathcal{S}})\right]\right\}.$$

The migration is done with the travel times $\tau(\mathbf{x}_r,\mathbf{y}^{\mathcal{S}})+\tau(\mathbf{x}_s,\mathbf{y}^{\mathcal{S}})$ of the waves from the source at $\mathbf{x}_s$ to the search point $\mathbf{y}^{\mathcal{S}}$ and then back to the receiver at $\mathbf{x}_r$. If the medium is homogeneous , $\tau(\mathbf{x},\mathbf{y}) = |\mathbf{x}-\mathbf{y}|/c_0$, with c_0 the propagation speed. In smoothly varying media with propagation speed $c(\mathbf{x})$, the travel time is given by

$$\tau(\mathbf{x},\mathbf{y}) = \min\int \frac{1}{c\left(\mathcal{X}(s)\right)}\,\mathrm{d}s$$

where the minimum is over all paths $\mathcal{X}$ that start at $\mathbf{x}$ and end at $\mathbf{y}$.

The KM functionals and their variants have been widely used in many applications such as non-destructive testing, seismic imaging and radar. In some applications such as in radar the background medium is homogeneous, but migration can be applied more generally in media with smooth velocity background.

Kirchhoff migration works well in homogeneous or smooth media where the waves are scattered significantly only at the reflectors which we want to image. The arrival times of the echoes are easy to identify as we can see from the time traces which are clean, being everywhere equal to zero except in the vicinity of the arrival times corresponding to the echoes from the reflectors (see Figure 2.2). In this case the

Kirchhoff migration functional peaks at the search points that have travel times near these arrival times.

We will first illustrate on some numerical examples the performance of KM imaging in homogeneous and inhomogeneous random media.

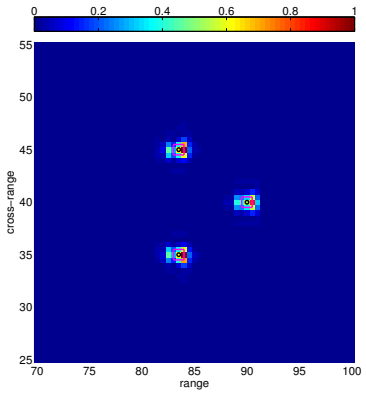

Figure 4.1: The Kirchhoff migration image of three reflectors in a homogeneous background.

When the background medium in which we wish to image has inhomogeneities this will drastically affect the wave propagation. As we can see in Figure 2.2 the time traces are not clean as in the previous case and the arrival times of the echoes are not easy to identify any more. Now the waves are scattered by the inhomogeneities of the medium and the time traces have a lot of delay spread or coda. The Kirchhoff migration images obtained in this case are not only noisy but also unstable with respect the realization of the medium inhomogeneities.

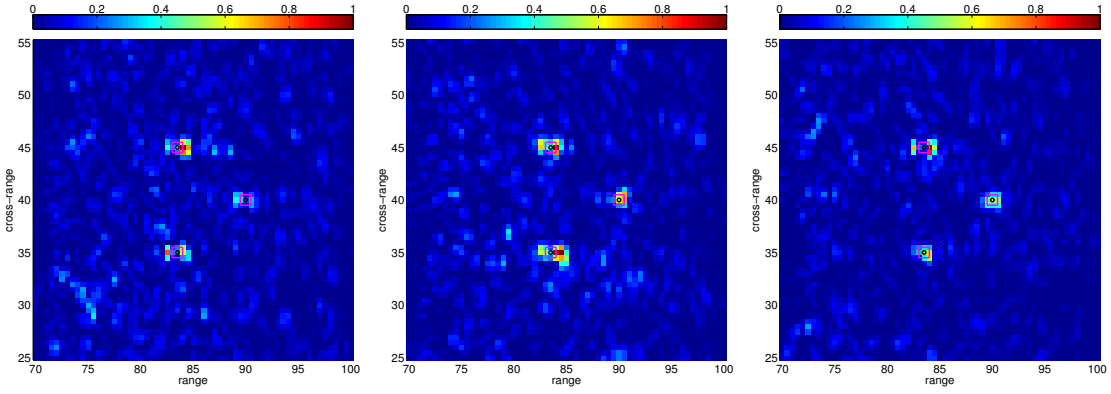

Figure 4.2: Kirchhoff migration images for three different realizations of the clutter, with the same statistical characteristics.

The stability of the images when imaging with Kirchhoff migration is also affected by the scatterers size and the scatterers reflectivity as we see in Figure 4.3 and Figure 4.4, respectively.

The index of refraction $n(\vec{\mathbf{x}}) = c_0/c(\vec{\mathbf{x}})$ in the objects we want to image is defined as $n(\vec{\mathbf{x}}) = \dfrac{c_0}{c_0 + \rho}$, where $\rho = 0.2, 0.4, 0.6$. This is for the Figure 4.4. In the other figures we use $\rho = 0.4$.

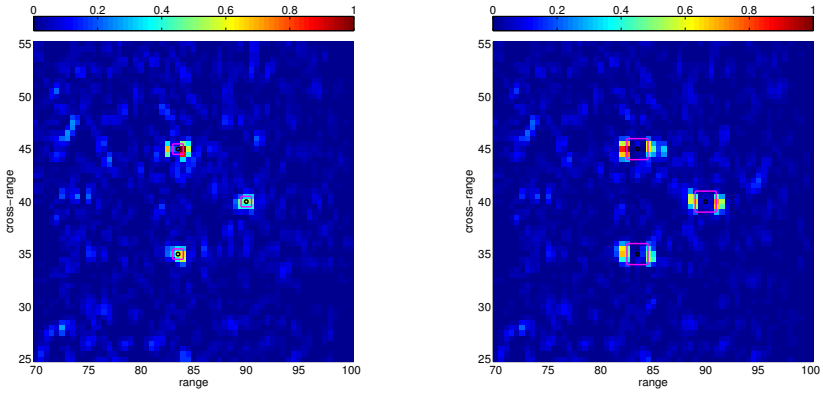

Figure 4.3: Kirchhoff migration images for the same realization of the clutter. The scatterers have the same reflectivity. *Left:*The scatterers size is $1\lambda_0$. *Right:*The scatterers size is $2\lambda_0$.

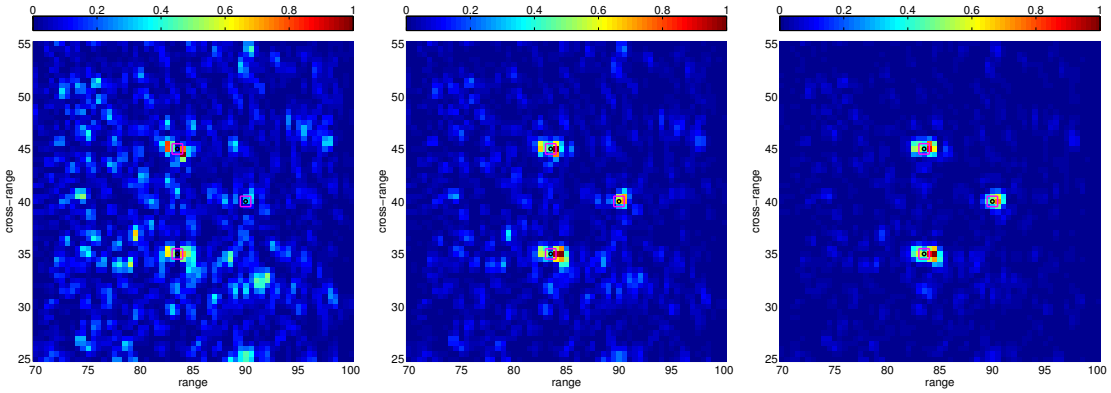

Figure 4.4: Kirchhoff migration images for the same realization of the clutter. The scatterers have the same size. The reflectivity of the scatterers increases from left to the right.

To make imaging work in clutter we need an efficient technique for compressing the delay spread in the traces. We consider this in the next section.

5 Coherent interferometry

An effective way to reduce the delay spread in the traces is to correlate them and obtain the interferograms

$$\begin{aligned} P(\mathbf{x}_r, \mathbf{x}_s, \cdot) *_t P(\mathbf{x}_{r'}, \mathbf{x}_s - \cdot)(t) &= \int \mathrm{d}t\, ' P(\mathbf{x}_r, \mathbf{x}_s, t') *_t P(\mathbf{x}_{r'}, \mathbf{x}_s, t' - t) \\ &= \frac{1}{2\pi} \int \mathrm{d}\omega\, \widehat{P}(\mathbf{x}_r, \mathbf{x}_s, \omega) \overline{\widehat{P}(\mathbf{x}_{r'} \mathbf{x}_s, \omega)} e^{-i\omega t} \end{aligned}$$

where the bar indicates complex conjugate. Also for simplicity we take the noisy traces produced with illumination from a single source located at $\mathbf{x}_s$.

The migration of the interferograms to the search points $\mathbf{y}^{\mathcal{S}}$ is done with the travel times computed in a smooth background that we assume is known. The interferometric imaging function is

$$\mathcal{I}^{\mathbf{INT}}(\mathbf{y}^{\mathcal{S}}) = \sum_{\mathbf{x}_r \mathbf{x}_{r'}} P(\mathbf{x}_r, \mathbf{x}_s, \cdot) *_t P(\mathbf{x}_{r'}, \mathbf{x}_s - \cdot) \mid_{\tau(\mathbf{x}_r, yS) - \tau(\mathbf{x}_{r'}, \mathbf{y}^{\mathcal{S}})} .$$

We evaluate the interferograms at the difference of the travel time because it will have a peak at the lag time when $\mathbf{y}^{\mathcal{S}}$ is near a reflector. In the frequency domain the imaging function becomes

$$\mathcal{I}^{\mathbf{INT}}(\mathbf{y}^{\mathcal{S}}) = \int_{-\infty}^{+\infty} \mathrm{d}\omega \left| \sum_{r=1}^{N_r} \widehat{P}(\mathbf{x}_r, \mathbf{x}_s, \omega) \exp\left\{ -i\omega [\tau(\mathbf{x}_r, \mathbf{y}^{\mathcal{S}}) + \tau(\mathbf{x}_s, \mathbf{y}^{\mathcal{S}})] \right\} \right|^2 .$$

If we have a very large array or multiple arrays that allow us to do geometric triangulation $\mathcal{I}^{\mathbf{INT}}$ can provide range resolution in clutter. Otherwise, $\mathcal{I}^{\mathbf{INT}}$ does not provide any range resolution [11, 12]. In order to recover range resolution, a coherent interferometric imaging (CINT) functional that uses all the residual coherence in the data was introduced [12].

The fluctuations in the background sound speed introduces random fluctuations in the phases of the recorded waves. Therefore when we back-propagate numerically the data in a homogeneous medium, the phase terms do not compensate each other. This leads to noise and instabilities in the image. The idea in order to mitigate this effect is to back-propagate windowed space-frequency correlations of the data. In $\mathcal{I}^{\mathbf{INT}}$ the recorded traces $\widehat{P}(\mathbf{x}_r, \mathbf{x}_s, \omega)$ are treated as if they are uncorrelated at different frequencies. CINT exploits the correlations of $\widehat{P}(\mathbf{x}_r, \mathbf{x}_s, \omega)$ and $\widehat{P}(\mathbf{x}_r, \mathbf{x}_s, \omega')$ at different frequencies and at different receivers. As a consequence, even with a small array, CINT provides good range resolution.

The coherent interferometric functional is given by

$$\begin{aligned} \mathcal{I}^{\mathbf{CINT}}(\mathbf{y}^{\mathcal{S}}; \Omega_d, k_d) &= \int\int_{|\omega - \omega'| \le \Omega_d} \mathrm{d}\omega\ \mathrm{d}\omega\, ' \sum_{r=1}^{N_r} \sum_{\substack{r'=1 \\ |\mathbf{x}_r - \mathbf{x}_{r'}| \le \mathcal{X}_d\left(\frac{\omega+\omega'}{2}\right)}}^{N_r} \widehat{P}(\mathbf{x}_r, \mathbf{x}_s, \omega) \overline{\widehat{P}(\mathbf{x}_{r'}, \mathbf{x}_s, \omega')} \\ &\exp\left\{ -i \left[\omega \left(\tau(\mathbf{x}_r, \mathbf{y}^{\mathcal{S}}) + \tau(\mathbf{x}_s, \mathbf{y}^{\mathcal{S}}) \right) - \omega' \left(\tau(\mathbf{x}_{r'}, \mathbf{y}^{\mathcal{S}}) + \tau(\mathbf{x}_s, \mathbf{y}^{\mathcal{S}}) \right) \right] \right\} . \end{aligned} \tag{5.1}$$

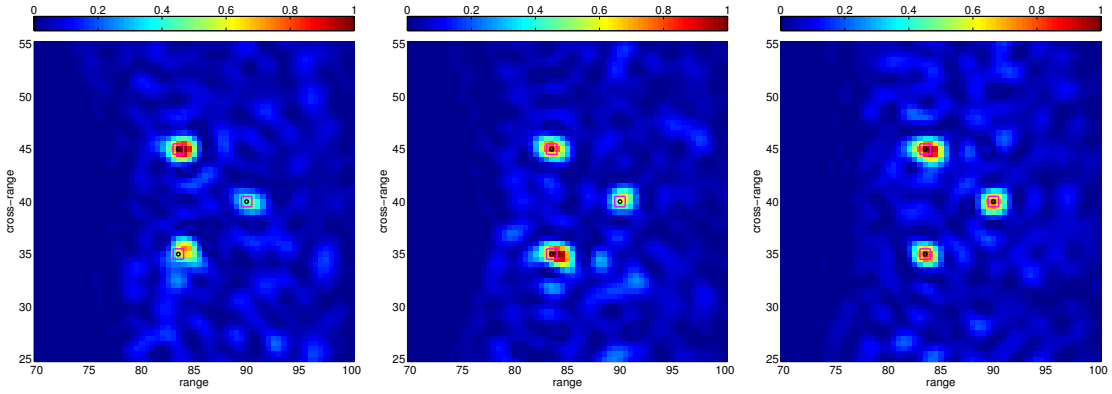

Figure 5.1: CINT images for three different realizations of the clutter, with the same statistical characteristics.

As we can see in Figure 5.1 the images we get with CINT are statistically stable and they do not depend on the realization of the clutter.

There are two characteristic coherence parameters in the data $\widehat{P}(\mathbf{x}_r, \mathbf{x}_s, \omega)$, the *decoherence frequency* Ω_d which is the difference in the frequencies ω and ω' over which $\widehat{P}(\mathbf{x}_r, \mathbf{x}_s, \omega)$ and $\widehat{P}(\mathbf{x}_r, \mathbf{x}_s, \omega')$ become uncorrelated, and the *decoherence length* $\mathcal{X}_d$ that is the difference in receiver locations $\mathbf{x}_r$ and $\mathbf{x}_{r'}$ over which $\widehat{P}(\mathbf{x}_{r'}, \mathbf{x}_s, \omega)$ and $\widehat{P}(\mathbf{x}_r, \mathbf{x}_s, \omega)$ become uncorrelated. The idea behind the CINT functional is that, at nearby frequencies ω, ω' and at nearby locations $\mathbf{x}_r, \mathbf{x}_{r'}$, the random phase shifts of the data $\widehat{P}(\mathbf{x}_r, \mathbf{x}_s, \omega)$, $\overline{\widehat{P}(\mathbf{x}_{r'}, \mathbf{x}_s, \omega')}$ are correlated, so they can approximately cancel each other in the product $\widehat{P}(\mathbf{x}_r, \mathbf{x}_s, \omega)\overline{\widehat{P}(\mathbf{x}_{r'}, \mathbf{x}_s, \omega')}$. Thus we can say that the data are coherent. In this case the back-propagation in the homogeneous medium will be stable. The CINT imaging function keeps the pairs $(\mathbf{x}_r, \omega)$ and $(\mathbf{x}_{r'}, \omega')$ for which the data are coherent and disregards the pairs that do not carry any coherent information. It then appears that the cut-off parameters Ω_d and $\mathcal{X}_d$ should be of the order of frequency and the spatial correlation length of the recorded data.

The decoherence frequency Ω_d depends on the clutter and the range L of the reflectors and when there is significant delay spread in the traces it can be much smaller than the bandwidth B. The decoherence length $\mathcal{X}_d$ is also determined by the clutter and the range L but it depends on the frequency as well. It can be estimated by

$$\mathcal{X}_d(\omega) = \frac{c_0}{\omega k_d} = \frac{c_0 L}{\omega a_e}$$

where a_e is the effective aperture in time reversal, and the dimensionless parameter k_d quantifies the uncertainty in the direction of arrival of the echoes in clutter. The estimation of those parameters is possible and it is not a simple task, it is best done adaptively [14]. Depending on the parameters Ω_d and $\mathcal{X}_d$, we get different trade-offs between stability and resolution.

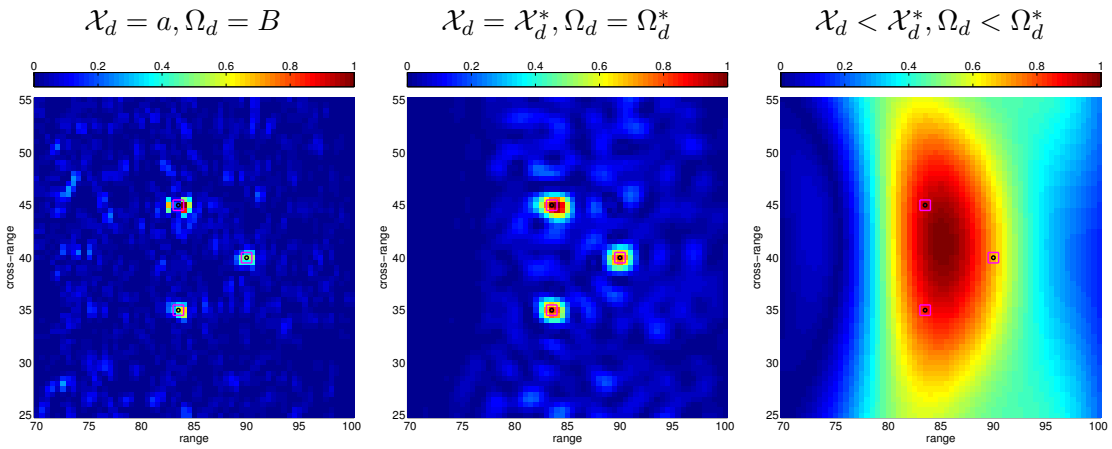

Figure 5.2: Coherent interferometry images in random media for different values of the parameters $\mathcal{X}_d$ and Ω_d.

Here we demonstrate with numerical simulations that the optimal decoherence parameters $\mathcal{X}_d^*$,Ω_d^* exist, by displaying in Figure 5.2 the images for $\mathcal{X}_d$,Ω_d larger, equal and smaller than $\mathcal{X}_d^*$,Ω_d^*, respectively. Note that $\mathcal{I}^{\mathbf{CINT}}$ is equal to the square of the Kirchhoff migration functional $\mathcal{I}^{\mathbf{KM}}$ when $\Omega_d = B$ and $\mathcal{X}_d = a$, that is when, there is no smoothing to account for the reduced coherence in the data. When the values of $\mathcal{X}_d$ and Ω_d are smaller than the optimal ones, the estimated image is over-smoothed, that is, blurrier that the optimal image.

In the following figures we show the effect of the parameters $\mathcal{X}_d$ and Ω_d, respectively, in the image resolution.

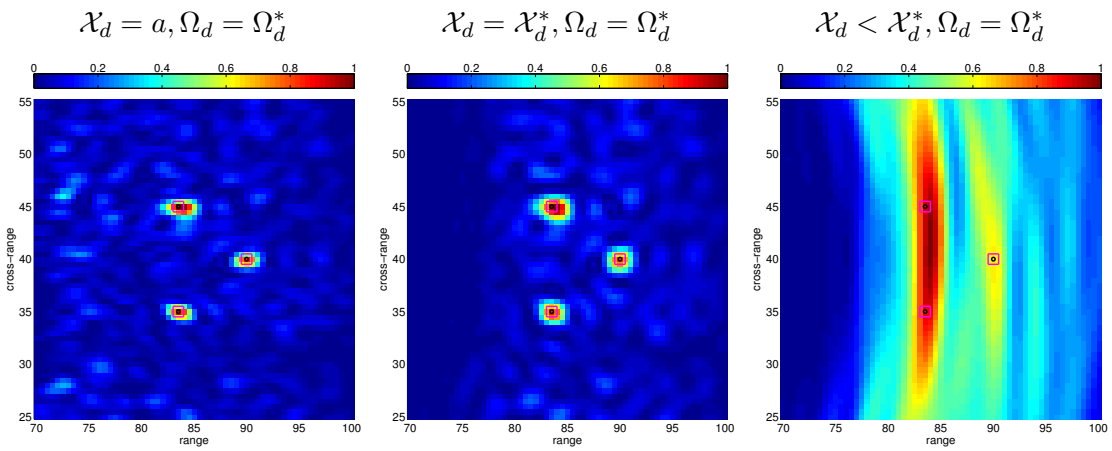

Figure 5.3: Coherent Interferometry: The effect of $\mathcal{X}_d$ on image resolution. The value of Ω_d is fixed and $\mathcal{X}_d$ decreases from left to right with the optimal in the middle.

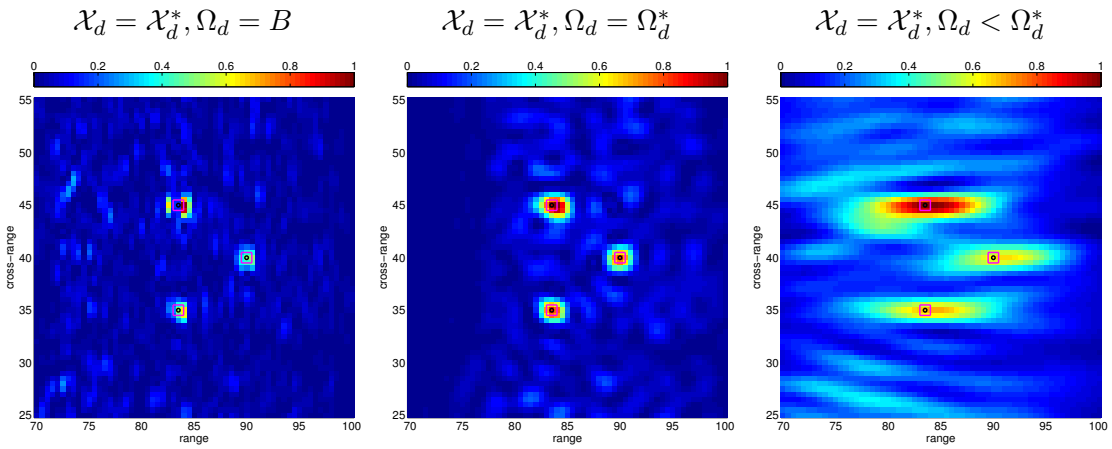

Figure 5.4: Coherent Interferometry: The effect of Ω_d on image resolution. The value of $\mathcal{X}_d$ is fixed and Ω_d decreases from left to right with the optimal in the middle.

Lets note that when we have full array data traces, that means, we probe the medium from each one of the array's element, the CINT function is

$$\mathcal{I}^{\mathbf{CINT}}(\mathbf{y}^{\mathcal{S}};\Omega_d,k_d) = \int\int_{|\omega-\omega'|\le\Omega_d} \mathrm{d}\omega\ \mathrm{d}\omega' \sum_{r=1}^{N_r}\sum_{r'=1}^{N_r} \sum_{s=1}^{N_s}\sum_{s'=1}^{N_s} \underset{|\mathbf{x}_r-\mathbf{x}_{r'}|\le\mathcal{X}_d\left(\frac{\omega+\omega'}{2}\right)}{\underset{|\mathbf{x}_s-\mathbf{x}_{s'}|\le\mathcal{X}_d\left(\frac{\omega+\omega'}{2}\right)}{}} \widehat{P}(\mathbf{x}_r,\mathbf{x}_s,\omega)\overline{\widehat{P}(\mathbf{x}_{r'},\mathbf{x}_{s'},\omega')} \times \exp\left\{-i\left[\omega\left(\tau(\mathbf{x}_r,\mathbf{y}^{\mathcal{S}})+\tau(\mathbf{x}_s,\mathbf{y}^{\mathcal{S}})\right)-\omega'\left(\tau(\mathbf{x}_{r'},\mathbf{y}^{\mathcal{S}})+\tau(\mathbf{x}_{s'},\mathbf{y}^{\mathcal{S}})\right)\right]\right\} \tag{5.2}$$

this will be useful in the next section.

6 Pixel scanning image formation with windowed energy beamformer

An alternative approach to array imaging that may be implemented efficiently in hardware is to form the image by beamforming to each point in the imaging window $\mathcal{I}_{\rm W}$ and compute the image pixel by pixel. The array uses successive multiple illuminations to beamform to each pixel $\mathbf{y}^{\mathcal{S}} \in \mathcal{I}_{\rm W}$, records the echoes and then synchronizes and adds them over the array to compute the value of the image at $\mathbf{y}^{\mathcal{S}}$. The synchronization is done with time delays computed relative to $\mathbf{y}^{\mathcal{S}}$ and the summation superposes coherently echoes from a possible scatter at $\mathbf{y}^{\mathcal{S}}$, which is called beamforming in reception.

Let $\mathbf{y}^{\mathcal{S}}$ be an arbitrary pixel in $\mathcal{I}_{\rm W}$, at which we form the image. The array beamforms at $\mathbf{y}^{\mathcal{S}}$ by emitting from its sources delayed pulses. The delays are computed so that all the pulses arrive at $\mathbf{y}^{\mathcal{S}}$ at the same time. The beamforming can involve all the sources at once, or it can work with sub-apertures. The sources can also be weighted to control focusing of the beam at $\mathbf{y}^{\mathcal{S}}$. After beamforming, the array receives the echoes from scattering in the vicinity of $\mathbf{y}^{\mathcal{S}}$.

Let us suppose that the array is linear in the two-dimensional case, or square planar in three dimensions. This allows us to introduce a system of coordinates with range axis originating from the array in the orthogonal direction. The sensor locations are $\vec{\mathbf{x}}_r = (\mathbf{x}_r, 0)$, with $\mathbf{x}_r$ in the array aperture $\mathcal{A} \subset \mathbb{R}^2$ for $r = 1, \ldots, N$. The aperture $\mathcal{A}$ is a line segment of length a in the two dimensions.

We model the sub-apertures and the sensor weights used in beamforming with a function $\psi(\xi)$ of dimensionless arguments in $\mathbb{R}^n$ and support $\xi \in [-1/2, 1/2]$ for $n = 1$ or $\xi \in [-1/2, 1/2] \times [-1/2, 1/2]$ for $n = 2$. The size of the sub-aperture is determined by the length $\mathcal{X}$ in the scaled version of ψ,

$$\psi_{\mathcal{X}}(\mathbf{x}) = \psi(\frac{\mathbf{x}}{\mathcal{X}}).$$

We denote by $P_{I(\mathbf{x}_s)}(t, \mathbf{x}_r; \mathbf{y}^{\mathcal{S}})$ the echoes received at $\mathbf{x}_r \in \mathcal{A}$ after beamforming from the sub-aperture centered at $\mathbf{x}_s \in \mathcal{A}$ on the pixel $\mathbf{y}^{\mathcal{S}}$. Its expression is

$$P_{I(\mathbf{x}_s)}(t, \mathbf{x}_r; \vec{\mathbf{y}}^S) = \sum_{\sigma=1}^{N} \psi_{\mathcal{X}}(\mathbf{x}_s - \mathbf{x}_\sigma) P(t + \tau(\mathbf{x}_\sigma, \vec{\mathbf{y}}^S) - \tau(\mathbf{x}_s, \vec{\mathbf{y}}^S), \vec{\mathbf{x}}_r, \vec{\mathbf{x}}_\sigma) \qquad (6.1)$$

where we changed slightly the notation of the travel time $\tau(\mathbf{x}_s, \vec{\mathbf{y}}^S)$ from $\vec{\mathbf{x}}_s = (\mathbf{x}_s, 0)$ to $\vec{\mathbf{y}}^S$, to emphasize its dependence on the cross-range source coordinate $\mathbf{x}_s$. For simplicity we assume that the array plays the dual role of sources and receivers. All the indices s, σ, r and ρ take values in the set $\{1, 2, \ldots, N\}$. We use now that the sources are indexed by s and σ and the receivers by r and ρ. The relative delays $\tau(\mathbf{x}_\sigma, \vec{\mathbf{y}}^S) - \tau(\mathbf{x}_s, \vec{\mathbf{y}}^S)$ are used in (6.1) to synchronize the arrivals at $\vec{\mathbf{y}}^S$ of the signals from all the sources in the support of $\psi_{\mathcal{X}}$, with center at $\mathbf{x}_s$. This is the *delay-and-sum* (DAS) beamforming process [24, 20], whose performance depends on the choice of the window function $\psi_{\mathcal{X}}$, the frequency band of the probing pulse $f(t)$, and the medium through which the waves propagate.

In smooth and known media the range resolution is determined by the precision with which the system can estimate travel times, that is by the pulse width. The larger the bandwidth, the shorter the time width of the pulse and the better the

resolution of the beamformer. The cross-range resolution is determined by the carrier wavelength λ_0, the range L of the pixel $\vec{\mathbf{y}}^S$ and the window function $\psi_{\mathcal{X}}$. The local beamforming in reception consists of synchronizing by travel time delays the received echoes $P_{I(\mathbf{x}_s)}(t, \mathbf{x}_r; \vec{\mathbf{y}}^S)$ and adding them over the receivers in sub-apertures centered at $\mathbf{x}_r$, with uniform or variable weights. We denote the result by $P_{R(\mathbf{x}_r),I(\mathbf{x}_s)}(t, ; \vec{\mathbf{y}}^S)$ and write its mathematical model as follows

$$P_{R(\mathbf{x}_r),I(\mathbf{x}_s)}(t; \vec{\mathbf{y}}^S) = \sum_{\rho=1}^{N} \psi_{\mathcal{X}}(\mathbf{x}_\rho - \mathbf{x}_r) P_{I(\mathbf{x}_s)}(t + \tau(\mathbf{x}_\rho, \vec{\mathbf{y}}^S) - \tau(\mathbf{x}_r, \vec{\mathbf{y}}^S), \mathbf{x}_\rho; \vec{\mathbf{y}}^S). \quad (6.2)$$

In general, the weights and sub-apertures may be different in reception than in emission. Note, the smaller $\mathcal{X}$ is, the more smoothing at the expense of resolution. We compute now the energy of $P_{R(\mathbf{x}_r),I(\mathbf{x}_s)}(t; \vec{\mathbf{y}}^S)$ over a properly chosen time window function $\phi_{\mathcal{T}}$ and sum over the sub-apertures to form the windowed beamformer energy (WBE) imaging function:

$$\mathcal{I}^{\mathbf{WBE}}(\vec{\mathbf{y}}^S; \mathcal{T}, \mathcal{X}) = \sum_{s,r} \int \frac{\mathrm{d}t}{2\pi} \left| \phi_{\mathcal{T}} \left(t - \tau(\mathbf{x}_r, \vec{\mathbf{y}}^S) - \tau(\mathbf{x}_s, \vec{\mathbf{y}}^S) \right) P_{R(\mathbf{x}_r),I(\mathbf{x}_s)}(t; \vec{\mathbf{y}}^S) \right|^2 . \quad (6.3)$$

The time window function is of the form

$$\phi_{\mathcal{T}}(t) = \mathcal{T}^{-1/2} \phi \left(\frac{t}{\mathcal{T}} \right).$$

It is the scaled version of a function $\phi(u)$ of dimensionless argument that is supported in the interval $|u| \leq 1/2$, with normalization so that

$$\int_{-\infty}^{+\infty} \frac{\mathrm{d}t}{2\pi} \phi_{\mathcal{T}}^2(t) = \int_{-\infty}^{+\infty} \frac{\mathrm{d}u}{2\pi} \phi^2(u).$$

For example, one may take $\phi(u) = \mathbf{1}_{[-1/2,1/2]}(u)$ which is equal to one when $|u| \leq 1/2$ and 0 otherwise. We take $\phi(u)$ to be a Gaussian function. The time window function $\phi_{\mathcal{T}}$ is used in (6.3) to evaluate the energy received at $\mathbf{x}_r$, over the time interval of length $\mathcal{T}$, centered at the travel time $\tau(\mathbf{x}_r, \vec{\mathbf{y}}^S) + \tau(\mathbf{x}_s, \vec{\mathbf{y}}^S)$, when the illumination is from the source at $\mathbf{x}_s$. The time $\mathcal{T}$ may be chosen small, comparable to the pulse width in homogeneous media. In cluttered media, $\mathcal{T}$ may be larger so as to account for the pulse delay spread, that is the arrival of the multiply scattered waves from the clutter.

6.1 Transformation of $\mathcal{I}^{\mathbf{WBE}}$ into back-propagated local cross-correlations

First, we change variables in the time integral in (6.3)

$$t \rightsquigarrow t + \tau(\mathbf{x}_r, \vec{\mathbf{y}}^S) + \tau(\mathbf{x}_s, \vec{\mathbf{y}}^S)$$

and using Parseval's identity obtain

$$\mathcal{I}^{\mathbf{WBE}}(\vec{\mathbf{y}}^S;\mathcal{T},\mathcal{X}) = \sum_{s,r}\int \frac{\mathrm{d}t}{2\pi}\left|P_{\mathcal{T},\mathcal{X}}(t,\mathbf{x}_r,\mathbf{x}_s;\vec{\mathbf{y}}^S)\right|^2$$
$$= \sum_{s,r}\int \mathrm{d}\omega\ \left|\widehat{P}_{\mathcal{T},\mathcal{X}}(\omega,\mathbf{x}_r,\mathbf{x}_s;\vec{\mathbf{y}}^S)\right|^2. \qquad (6.4)$$

Here we have defined

$$P_{\mathcal{T},\mathcal{X}}(t,\mathbf{x}_r,\mathbf{x}_s;\vec{\mathbf{y}}^S) = \phi_{\mathcal{T}}(t)P_{R(\mathbf{x}_r),I(\mathbf{x}_s)}(t+\tau(\mathbf{x}_r,\vec{\mathbf{y}}^S)+\tau(\mathbf{x}_s,\vec{\mathbf{y}}^S);\vec{\mathbf{y}}^S)$$

and we recall from equations (6.1) and (6.2) that

$$P_{R(\mathbf{x}_r),I(\mathbf{x}_s)}(t+\tau(\mathbf{x}_r,\vec{\mathbf{y}}^S)+\tau(\mathbf{x}_s,\vec{\mathbf{y}}^S);\vec{\mathbf{y}}^S) = \sum_{\rho,\sigma}\psi_{\mathcal{X}}(\mathbf{x}_\sigma-\mathbf{x}_s)\psi_{\mathcal{X}}(\mathbf{x}_\rho-\mathbf{x}_r)$$
$$\times P(t+\tau(\mathbf{x}_\rho,\vec{\mathbf{y}}^S)+\tau(\mathbf{x}_\sigma,\vec{\mathbf{y}}^S),\vec{\mathbf{x}}_\rho,\vec{\mathbf{x}}_\sigma).$$

In the frequency domain we have the convolution

$$\widehat{P}_{\mathcal{T},\mathcal{X}}(\omega,\vec{\mathbf{x}}_r,\vec{\mathbf{x}}_s;\vec{\mathbf{y}}^S) = \int \frac{\mathrm{d}\omega'}{2\pi}\widehat{\phi_{\mathcal{T}}}(\omega-\omega')\sum_{\rho,\sigma}\psi_{\mathcal{X}}(\mathbf{x}_\sigma-\mathbf{x}_s)\psi_{\mathcal{X}}(\mathbf{x}_\rho-\mathbf{x}_r)$$
$$\times\widehat{P}(\omega',\vec{\mathbf{x}}_\rho,\vec{\mathbf{x}}_\sigma)\exp\left\{-i\omega'\left[\tau(\mathbf{x}_\rho,\vec{\mathbf{y}}^S)+\tau(\mathbf{x}_\sigma,\vec{\mathbf{y}}^S))\right]\right\}$$

and the imaging function becomes

$$\mathcal{I}^{\mathbf{WBE}}(\vec{\mathbf{y}}^S;\mathcal{T},\mathcal{X}) = \sum_{s,r}\sum_{\rho,\rho'}\psi_{\mathcal{X}}(\mathbf{x}_\rho-\mathbf{x}_r)\psi_{\mathcal{X}}(\mathbf{x}_{\rho'}-\mathbf{x}_r)\sum_{\sigma,\sigma'}\psi_{\mathcal{X}}(\mathbf{x}_\sigma-\mathbf{x}_s)\psi_{\mathcal{X}}(\mathbf{x}_{\sigma'}-\mathbf{x}_s)$$
$$\times\int \mathrm{d}\omega\int\frac{\mathrm{d}\omega'}{2\pi}\int\frac{\mathrm{d}\omega''}{2\pi}\widehat{\phi_{\mathcal{T}}}(\omega-\omega')\overline{\widehat{\phi_{\mathcal{T}}}(\omega-\omega'')}\widehat{P}(\omega',\vec{\mathbf{x}}_\rho,\vec{\mathbf{x}}_\sigma)\overline{\widehat{P}(\omega'',\vec{\mathbf{x}}_{\rho'},\vec{\mathbf{x}}_{\sigma'})}$$
$$\times\exp\left\{-i\omega'\left[\tau(\mathbf{x}_\rho,\vec{\mathbf{y}}^S)+\tau(\mathbf{x}_\sigma,\vec{\mathbf{y}}^S)\right]+i\omega''\left[\tau(\mathbf{x}_{\rho'},\vec{\mathbf{y}}^S)+\tau(\mathbf{x}_{\sigma'},\vec{\mathbf{y}}^S)\right]\right\}. \qquad (6.5)$$

Now we use the convolution identity

$$\int\frac{\mathrm{d}\omega}{2\pi}\widehat{\phi_{\mathcal{T}}}(\omega-\omega')\overline{\widehat{\phi_{\mathcal{T}}}(\omega-\omega'')} = \int \mathrm{d}t\ |\phi_{\mathcal{T}}(t)|^2\,e^{i(\omega''-\omega')t} = \int \mathrm{d}t\ |\phi(t)|^2\,e^{i\mathcal{T}\omega t}.$$

If we define the new frequency window function Φ by

$$\Phi(t) = |\phi(t)|^2, \qquad \widehat{\Phi}(\omega) = \int \mathrm{d}t\ |\phi(t)|^2 e^{i\omega t}, \qquad (6.6)$$

then we have

$$\int\frac{\mathrm{d}\omega}{2\pi}\widehat{\phi_{\mathcal{T}}}(\omega-\omega')\overline{\widehat{\phi_{\mathcal{T}}}(\omega-\omega'')} = \widehat{\Phi}\left[\mathcal{T}(\omega''-\omega')\right].$$

We also introduce the spatial window function Ψ defined by

$$\Psi\left(\frac{\mathbf{x}_{\rho'}-\mathbf{x}_{\rho}}{\mathcal{X}}\right) = \sum_r \psi_{\mathcal{X}}(\mathbf{x}_\rho-\mathbf{x}_r)\psi_{\mathcal{X}}(\mathbf{x}_{\rho'}-\mathbf{x}_r)$$
$$= \sum_r \psi\left(\frac{\mathbf{x}_\rho-\mathbf{x}_r}{\mathcal{X}}\right)\psi\left(\frac{\mathbf{x}_{\rho'}-\mathbf{x}_\rho}{\mathcal{X}}+\frac{\mathbf{x}_\rho-\mathbf{x}_r}{\mathcal{X}}\right). \qquad (6.7)$$

With this notations we obtain the following expression of the windowed beamformer energy function

$$\mathcal{I}^{\mathbf{WBE}}(\vec{\mathbf{y}}^S;\mathcal{T},\mathcal{X}) = \frac{1}{2\pi}\int \mathrm{d}\omega \int \mathrm{d}\omega\, '\widehat{\Phi}\left[\mathcal{T}(\omega'-\omega)\right]\sum_{\rho,\rho'}\Psi\left(\frac{\mathbf{x}_{\rho'}-\mathbf{x}_\rho}{\mathcal{X}}\right)$$
$$\times\sum_{\sigma,\sigma'}\Psi\left(\frac{\mathbf{x}_{\sigma'}-\mathbf{x}_\sigma}{\mathcal{X}}\right)\widehat{P}(\omega,\vec{\mathbf{x}}_\rho,\vec{\mathbf{x}}_\sigma)\overline{\widehat{P}(\omega',\vec{\mathbf{x}}_{\rho'},\vec{\mathbf{x}}_{\sigma'})}$$
$$\times\exp\left\{-i\omega\left[\tau(\mathbf{x}_\rho,\vec{\mathbf{y}}^S)+\tau(\mathbf{x}_\sigma,\vec{\mathbf{y}}^S)\right]+i\omega'\left[\tau(\mathbf{x}_{\rho'},\vec{\mathbf{y}}^S)+\tau(\mathbf{x}_{\sigma'},\vec{\mathbf{y}}^S)\right]\right\}. \qquad (6.8)$$

6.2 Connection between the $\mathcal{I}^{\mathbf{WBE}}$ and the $\mathcal{I}^{\mathbf{CINT}}$ imaging function.

Let us introduce another expression of the CINT imaging function, so that it is easier to compare it with the windowed beamformer energy imaging function. We rewrite the $\mathcal{I}^{\mathbf{CINT}}$ imaging function as:

$$\mathcal{I}^{\mathbf{CINT}}(\vec{\mathbf{y}}^S;\mathcal{T}^C,\mathcal{X}^C) = \frac{1}{2\pi}\int \mathrm{d}\omega \int \mathrm{d}\omega\, '\widehat{\Phi}^C\left[\mathcal{T}^C(\omega''-\omega')\right]\sum_{\rho,\rho'}\Psi^C\left(\frac{\mathbf{x}_{\rho'}-\mathbf{x}_\rho}{\mathcal{X}^C\left(\frac{\omega+\omega'}{2}\right)}\right)$$
$$\times\sum_{\sigma,\sigma'}\Psi^C\left(\frac{\mathbf{x}_{\sigma'}-\mathbf{x}_\sigma}{\mathcal{X}^C\left(\frac{\omega+\omega'}{2}\right)}\right)\widehat{P}(\omega,\vec{\mathbf{x}}_\rho,\vec{\mathbf{x}}_\sigma)\overline{\widehat{P}(\omega',\vec{\mathbf{x}}_{\rho'},\vec{\mathbf{x}}_{\sigma'})}$$
$$\times\exp\left\{-i\omega\left[\tau(\mathbf{x}_\rho,\vec{\mathbf{y}}^S)+\tau(\mathbf{x}_\sigma,\vec{\mathbf{y}}^S)\right]+i\omega'\left[\tau(\mathbf{x}_{\rho'},\vec{\mathbf{y}}^S)+\tau(\mathbf{x}_{\sigma'},\vec{\mathbf{y}}^S)\right]\right\}. \qquad (6.9)$$

Here $\widehat{\Phi}^C$ and Ψ^C are the frequency and the spatial window functions of dimensionless arguments and finite support. These window functions do not need to be the same as in (6.6) and (6.7), although we show that it is desirable that they are. The threshold parameters $\mathcal{T}^C$ and $\mathcal{X}^C$ scale the support of the window functions and we may let $\mathcal{X}^C$ vary with frequency, as in the equation (6.9). One can see the analogy between the equation (5.2) and equation (6.9).

Now we can relate the pixel scanning windowed beamformer energy function $\mathcal{I}^{\mathbf{WBE}}$ to $\mathcal{I}^{\mathbf{CINT}}$. We have

$$\mathcal{I}^{\mathbf{CINT}}(\vec{\mathbf{y}}^S;\mathcal{T}^C,\mathcal{X}^C) = \mathcal{I}^{\mathbf{WBE}}(\vec{\mathbf{y}}^S;\mathcal{T},\mathcal{X}),$$

if $\mathcal{T}^C=\mathcal{T}$, $\mathcal{X}^C(\omega)=\mathcal{X}$ for all ω in the bandwidth of the pulse, and if the window functions Φ^C and Ψ^C in CINT satisfy

$$\widehat{\Phi}^C(\tilde{\omega}) = \int \mathrm{d}u\,|\phi(u)|^2 e^{i\tilde{\omega}u} = \int \frac{\mathrm{d}\tilde{\omega}'}{2\pi}\widehat{\phi}(\tilde{\omega}+\tilde{\omega}')\overline{\widehat{\phi}(\tilde{\omega}')},$$

and

$$\Psi^C\left(\frac{\mathbf{x}_{\rho'}-\mathbf{x}_{\rho}}{\mathcal{X}}\right)=\sum_r \psi\left(\frac{\mathbf{x}_{\rho}-\mathbf{x}_{r}}{\mathcal{X}}\right)\psi\left(\frac{\mathbf{x}_{\rho'}-\mathbf{x}_{\rho}}{\mathcal{X}}+\frac{\mathbf{x}_{\rho}-\mathbf{x}_{r}}{\mathcal{X}}\right).$$

That means that $\mathcal{I}^{\mathbf{CINT}}$ and $\mathcal{I}^{\mathbf{WBE}}$ are mathematically equivalent only if the sensor threshold does not vary over the bandwidth $\left(\mathcal{X}^C(\omega)=\mathcal{X}\right)$. Then the results in [14, 16] indicate that $\mathcal{I}^{\mathbf{CINT}}$ and therefore $\mathcal{I}^{\mathbf{WBE}}$ is stable with respect to the realizations of the clutter if the thresholding parameters satisfy the bounds

$$\frac{1}{\mathcal{T}}\leq\Omega_d,\qquad \mathcal{X}\leq X_d(\omega)$$

for all ω in the pulse bandwidth.

In the Figure 6.1 are illustrated images of the same cluttered media with different values of the smoothing parameters for both imaging functions, $\mathcal{I}^{\mathbf{CINT}}$ and $\mathcal{I}^{\mathbf{WBE}}$, to show their equivalence. From this point on we use a slightly different numerical setup. We probe the medium using 26 sources and record the echoes on the collocated receivers, this is $N_s=N_r=26$. The array aperture is the same as before but the density of the elements on the array is changed. The distance between the used elements is now $2.5\lambda_0$ instead of $0.5\lambda_0$.

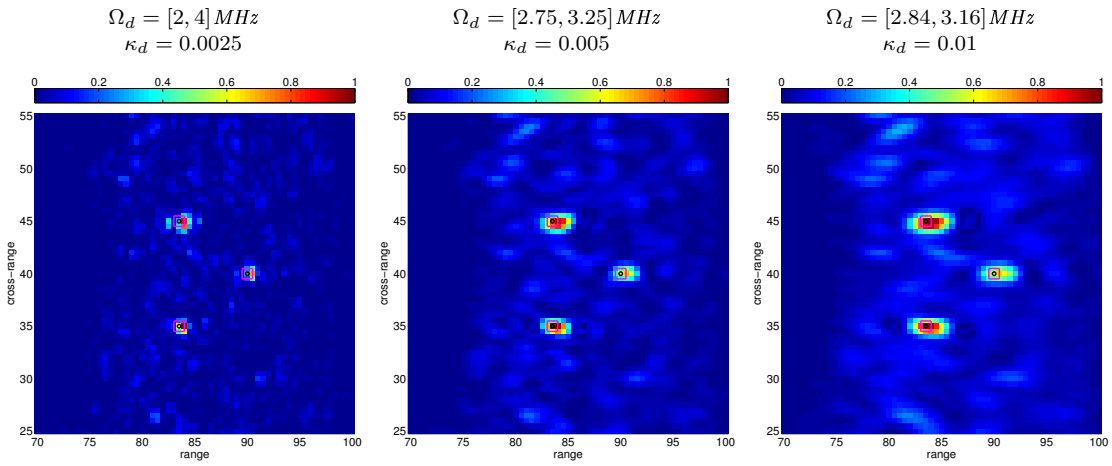

(a) *Coherent interferometry images.*

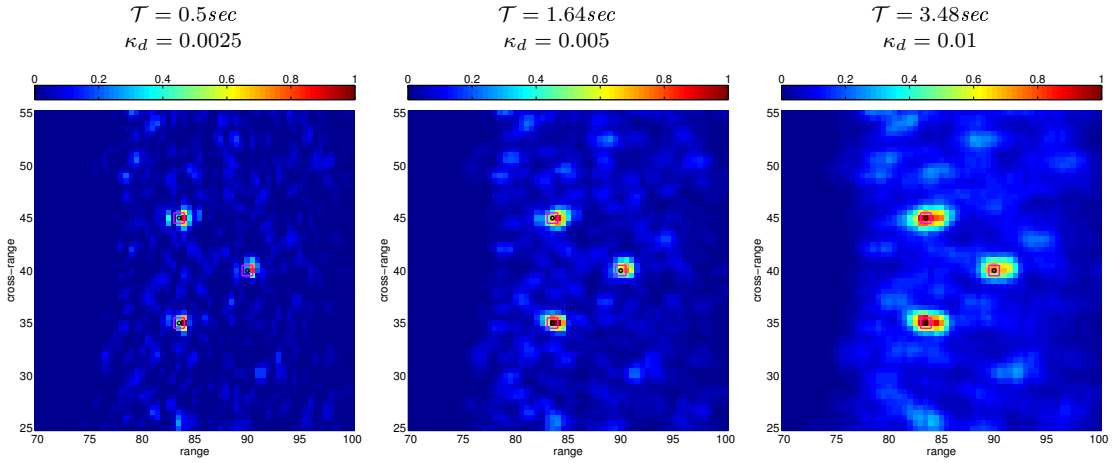

(b) *Window beam-forming images.*

Figure 6.1: The equivalence of the windowed beamformer energy imaging function to the coherent interferometric imaging function for different values of the smoothing parameters.

6.3 The algorithm

In this section we summarize the algorithm used for the implementation of the windowed beamformer energy imaging functional. We start the computation from the array response matrix, which is an $N_r \times N_s \times N_t$ matrix

$$\mathbb{P}(t) = \left(P(t, \vec{\mathbf{x}}_r, \vec{\mathbf{x}}_s)\right)_{r,s=1,\ldots,N} \ , \qquad t \in (0, t_f]$$

1. First we perform a smoothing in the edges of $\mathbb{P}$ in variables $\vec{\mathbf{x}}_r$ and $\vec{\mathbf{x}}_s$ with a Gaussian like function.

2. For each point $\vec{\mathbf{y}}^S$ in the image we compute the window of the data in the vicinity of the travel time $\tau(\vec{\mathbf{x}}_r, \vec{\mathbf{y}}^S) + \tau(\vec{\mathbf{x}}_s, \vec{\mathbf{y}}^S)$. This is compute

$$P_{\mathcal{T}}(t, \vec{\mathbf{x}}_r, \vec{\mathbf{x}}_s; \vec{\mathbf{y}}^S) = \phi_{\mathcal{T}}\left(t - \tau(\vec{\mathbf{x}}_r, \vec{\mathbf{y}}^S) - \tau(\vec{\mathbf{x}}_s, \vec{\mathbf{y}}^S)\right) P(t, \vec{\mathbf{x}}_r, \vec{\mathbf{x}}_s)$$

To reduce memory requirements we do not save the whole object, we shift this object to zero. For each point $\vec{\mathbf{y}}^S$ we compute

$$\tilde{P}_{\mathcal{T}}(t, \vec{\mathbf{x}}_r, \vec{\mathbf{x}}_s; \vec{\mathbf{y}}^S) = P_{\mathcal{T}}\left(t - \tau(\vec{\mathbf{x}}_r, \vec{\mathbf{y}}^S) - \tau(\vec{\mathbf{x}}_s, \vec{\mathbf{y}}^S), \vec{\mathbf{x}}_r, \vec{\mathbf{x}}_s; \vec{\mathbf{y}}^S\right) \tag{6.10}$$

The dimension of $\tilde{P}_{\mathcal{T}}$ in time is $N_{\mathcal{T}}$, which is the size of the window function $\phi_{\mathcal{T}}$. Now we do the Fourier transform of $\tilde{P}_{\mathcal{T}}(t, \vec{\mathbf{x}}_r, \vec{\mathbf{x}}_s; \vec{\mathbf{y}}^S)$ in time and we save

$$\widehat{P}_{\mathcal{T}}(\omega, \vec{\mathbf{x}}_r, \vec{\mathbf{x}}_s; \vec{\mathbf{y}}^S) = FFT\left(\tilde{P}_{\mathcal{T}}(t, \vec{\mathbf{x}}_r, \vec{\mathbf{x}}_s; \vec{\mathbf{y}}^S)\right)$$

The size of $\widehat{P}_{\mathcal{T}}$ is $N_{\mathcal{T}} \times N_r \times N_s \times N_I$,where N_I is the number of points in the image window.

3. Now we compute the 2d Fourier transform of $\widehat{P}_{\mathcal{T}}(\omega, \vec{\mathbf{x}}_r, \vec{\mathbf{x}}_s; \vec{\mathbf{y}}^S)$ in the variables $\vec{\mathbf{x}}_r$ and $\vec{\mathbf{x}}_s$. Lets call the resulting matrix

$$\widehat{Q}_{\mathcal{T}}(\omega, k_r, k_s; \vec{\mathbf{y}}^S) = FFT2\left(\widehat{P}_{\mathcal{T}}(\omega, \vec{\mathbf{x}}_r, \vec{\mathbf{x}}_s; \vec{\mathbf{y}}^S)\right)$$

4. After, we multiply the matrix $\widehat{Q}_{\mathcal{T}}$, in Fourier domain, with the window function $\psi_{\mathcal{X}}$. Here $\mathcal{X}$ is chosen to be independent of frequency and we take $\mathcal{X} = \mathcal{X}(\omega_0)$

$$\tilde{Q}_{\mathcal{T}}(\omega, k_r, k_s; \vec{\mathbf{y}}^S) = \widehat{Q}_{\mathcal{T}}(\omega, k_r, k_s; \vec{\mathbf{y}}^S)\widehat{\psi}_{\mathcal{X}}(k_r)\widehat{\psi}_{\mathcal{X}}(k_s)$$

5. The windowed beamformer energy image is the L^2 norm of $\tilde{Q}_{\mathcal{T}}(\omega, k_r, k_s; \vec{\mathbf{y}}^S)$, that is

$$\mathcal{I}^{\mathbf{WBE}}(\vec{\mathbf{y}}^S) = \sum_{k_r}\sum_{k_s}\int \mathrm{d}\omega \ \left|\tilde{Q}_{\mathcal{T}}(\omega, k_r, k_s; \vec{\mathbf{y}}^S)\right|^2 \tag{6.11}$$

6.4 Code performance and memory usage

As shown previously, the windowed beamformer energy function, with a proper set of smoothing parameters, can be equivalent to the coherent interferometric imaging function. The numerical results we presented in Figure 6.1 confirm this equivalence. Although the images we obtain by both methods are almost identical, an analysis of the performance for both methods shows that WBE can be computed much faster. It is also easy to see that WBE requires more memory then CINT.

The performance of WBE and CINT has been investigated for different values of the smoothing parameters. The performance tests have been addressed in the same computer, both imaging methods are written in Matlab®. We observed the computational time each imaging method needed to form the image and also the memory each method used during the computation. We present the results of those tests in the following figures.

First we observe that the computational time is not affected by the value of the cross-range smoothing parameter.

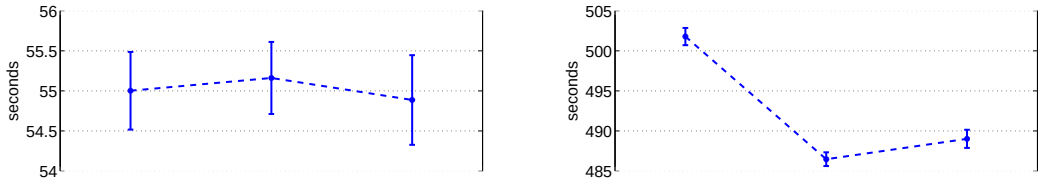

(a) *WBE imaging function.* **(b)** *CINT imaging function.*

Figure 6.2: Mean computational times in seconds for three different values of cross-range smoothing parameter $\kappa_d = 0.05, 0.005, 0.0025$.

We have to note here that the dimensionless parameter κ_d is used to compute the decoherence length $\mathcal{X}$. The decoherence length $\mathcal{X}$ when using the windowed beamformer energy imaging function is given by $\mathcal{X} = \frac{c_0}{\omega_0 \kappa_d}$ and the corresponding values that $\mathcal{X}$ takes in Figure 6.2a are: $\mathcal{X} = 3.1831$mm, $\mathcal{X} = 31.831$mm, $\mathcal{X} = 63.662$mm. The decoherence length used in the coherent interferometric function in Figure 6.2b is frequency dependent and its values are: $\mathcal{X}(\omega) \in [2.3873, 4.7746]$mm, $\mathcal{X}(\omega) \in [23.8732, 47.7465]$mm, $\mathcal{X}(\omega) \in [47.7465, 95.4930]$mm, calculated using the expression $\mathcal{X}(\omega) = \dfrac{c_0}{\omega \kappa_d}$.

Although the value of the cross-range smoothing parameter does not affect the performance of the methods, the value of the range smoothing parameter affects the computational times, as is shown in Figure 6.3.

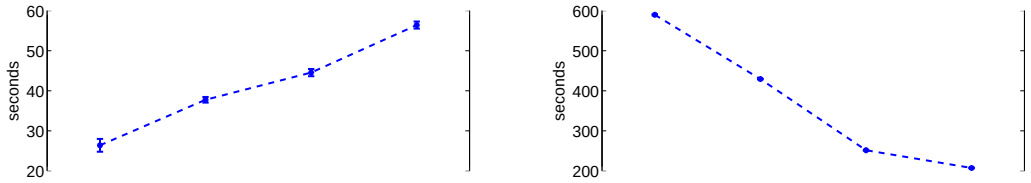

(a) *WBE imaging function.* **(b)** *CINT imaging function.*

Figure 6.3: Mean computational times in seconds for four different values of the range smoothing parameters $\mathcal{T}$ and Ω_d.

The time windows we used in Figure 6.3a are: $\mathcal{T} = 0.1155\mu$sec, $\mathcal{T} = 1.5856\mu$sec, $\mathcal{T} = 2.6356\mu$sec and $\mathcal{T} = 4.2107\mu$sec. The decoherence frequencies used in Figure 6.3b are: $\Omega_d = [2, 4]$MHz, $\Omega_d = [2.5, 3.5]$MHz, $\Omega_d = [2.75, 3.25]$MHz and $\Omega_d = [2.8, 3.2]$MHz.

In WBE, the bigger the size $\mathcal{T}$ of the time window, the smoother the image and the greater the computational time required. In CINT, the smaller the decoherence frequency Ω_d, the smoother the image and the lesser the computational time.

Comparing Figure 6.2a to Figure 6.2b and Figure 6.3a to Figure 6.3b we deduce that CINT is computationally ten times more expensive that the windowed beamformer energy function. The difference of computational times between the two methods is remarkable. The windowed beamformer energy function can be implemented efficiently both in hardware and software, that is, at a computational cost that is comparable to the usual beamforming and migration imaging methods. The performance of the Kirchhoff migration imaging function was also explored and we found that the mean computational time required was 18.3 seconds.

In our setups we found that the memory required by both methods was comparable, although we have to note that the required memory by WBE increases faster than the required memory by CINT when we try to image with larger arrays or/and more points in the imaging window. Let us explain further.

In the implementation of the windowed beamformer energy imaging function, the biggest matrix we have to save is the matrix $\widehat{P}_T$ of dimensions $N_T \times N_r \times N_s \times N_I$, where N_T is the discretization of the time window, N_r, N_s is the number receivers and sources we use and N_I is the number of pixels in the image window.

In the implementation of CINT, the biggest matrix we save has dimensions $N_B \times N_{\Omega_d} \times N_I$, where N_B is the number of frequencies in the available bandwidth and N_{Ω_d} the corresponding ones in Ω_d. Since $B > \Omega_d$ we also have $N_B > N_{\Omega_d}$. We note however that CINT can be implemented without using this matrix in which case the only memory required is that for saving the array response matrix and its Fourier transform (this will increase the computational time).

In the shown images, the number of pixels is $N_I = 3600$ for all the methods. The number of sensors used is $N_r = N_s = 26$. The length of the time window we used in WBE takes values in the interval $N_T \in [41, 401]$. The number of frequencies in the whole bandwidth is $N_B = 149$ and the number of frequencies used by the coherent interferometric imaging functional is $N_{\Omega_d} = \lfloor \frac{149}{n} \rfloor$, for different values of $n = 1, 2, 4, 5$, as shown in Figure 6.3.

Note that, to save a double-precision array of dimensions 1×1 the required memory is 8Bytes.

7 Multiple scattering, strong clutter and filtering

When imaging in unknown strongly scattering media with sound waves, an important issue is the multiple scattering of the waves by the medium heterogeneities. In most imaging techniques, including those that have been considered in this thesis, the data are collected in the following way: One or more transducers in the array emit a sound wave to the media to be imaged. The incident wave is reflected by the medium heterogeneities and the backscattered echoes are recorded by all sensors on the array. The backscattered wave contains two contributions: (i) The single scattering contribution, in which the incident wave has undergone one scattering event before coming back to the sensors. This is the contribution which we usually take in account in imaging by exploiting the relation between the arrival time of the echo and the distance between the scatterer and the sensors. Therefore an image of the medium's reflectivity can be formed from the recorded signals. (ii)The multiple scattering contribution, in which the wave undergoes several scattering events before being recorded to the sensors. Multiple scattering takes place when the medium heterogeneities are strong. These multiple scattered waves may arrive at the array long before and after the direct echoes from the scatterers. Because of multiple scattering there is not any more a direct relation between travel time and depth, which makes the localization of the echoes impossible above a few scattering mean-free paths. In this case the wave loses its coherence. The imaging techniques we used previously, namely Kirchhoff migration, WBE and CINT rely on a single scattering assumption, like most of the wide used techniques. Multiple scattering is a big issue in techniques based on the first Born approximation. This entails the need of carefully designed data filters, which will be able to decrease the multiple scattering effect.

7.1 State of the art and available methodology

A filter for removing contributions of multiple backscattered waves by randomly layered media was proposed and studied in [8]. It is an efficient filter, but since it relies on the layered structure of the random medium it does not generalize to other types of clutter. A more general filter that relies on the Local Cosine Transform (LCT) of the array response matrix was proposed in [17] and analyzed in [1]. In this case the time window that contains the coherent scattered field from the reflectors to be imaged is found by looking at the behavior of the largest singular values of the matrix of the local cosine coefficients. In windows that contain only clutter echoes the largest singular values are clustered together while in the windows that contain reflections from a coherent scatterer the largest singular value (possibly two) behaves differently from the other ones, especially for the lower frequencies. This allows for detecting the window that contains the coherent echoes. Filtering is then preformed by projecting the data on the subspace generated by the singular vectors corresponding to those larger singular values that behave differently from the rest. This LCT based methodology is a robust time-frequency selection procedure that is adaptive and data driven.

In [2, 3] the authors proposed another approach for dealing with multiple scattering. The filter they designed seeks to separate single from multiple scattering waves by performing a rotation of the response matrix followed by a projection. It

has been shown that the single scattering part of the data in the frequency domain is approximately a Hankel matrix. After the rotation the filtering is carried out by a projection on the space of certain rank one matrices. The single scattering filter plays no role when imaging with Kirchhoff migration but good results can be obtained by applying the DORT method to the filtered data. DORT is an acronym that stands for Decomposition de l'Operateur de Retournement Temporel. The DORT method [21] consists in computing the singular value decomposition of the array response matrix in the frequency domain. In the case of small point-like scatterers that are far apart from each other, it can be shown that there is an one-to-one correspondence between the significant singular values of the array response matrix and the scatterers. Selective focusing to each one of the scatterers can be achieved by backpropagating one by one the singular vectors corresponding to the significant singular values. In the case of the single scattering filter, DORT is applied on the filtered array response matrix.

The single scattering filter exploits the known deterministic dependence of the single scattered field on the difference variable $\vec{\mathbf{x}}_s - \vec{\mathbf{x}}_r$. This relation implies that the Fourier transform of the array response matrix is a Hankel matrix, that means it is constant along the anti-diagonals. To illustrate this we plotted in Figure 7.1 the Fourier transform of the recorded data $\widehat{P}(\omega, \vec{\mathbf{x}}_s, \vec{\mathbf{x}}_r)$ at the central frequency ω_0 in the plane $(\vec{\mathbf{x}}_s, \vec{\mathbf{x}}_r)$. On the left we show the scattered field corresponding to three scatterers in a homogeneous medium, while on the right we show the scattered field in an inhomogeneous medium with multiple scattering. On the left plot we observe a deterministic coherence along the anti-diagonals of the matrix $\widehat{P}(\omega, \vec{\mathbf{x}}_s, \vec{\mathbf{x}}_r)$, whereas on the right plot corresponding to inhomogeneous multiple scattering regime the matrix $\widehat{P}(\omega, \vec{\mathbf{x}}_s, \vec{\mathbf{x}}_r)$ seems to be random.

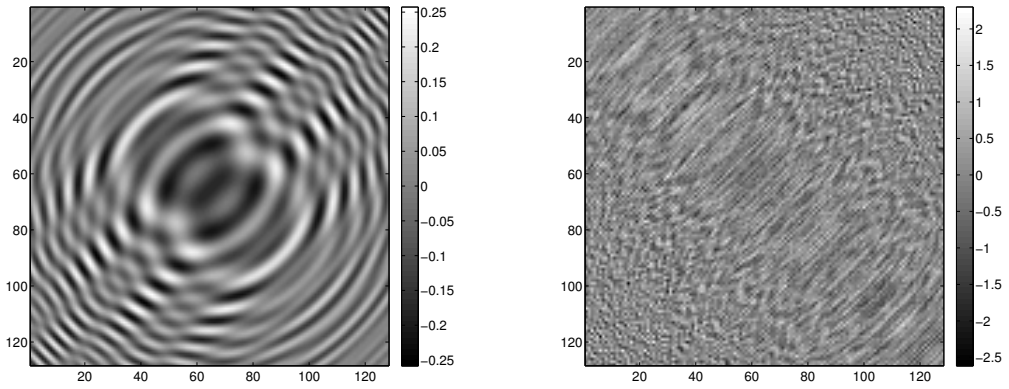

(a) *Homogeneous background.* **(b)** *Inhomogeneous background.*

Figure 7.1: Real part of the matrix $\widehat{P}(\omega, \vec{\mathbf{x}}_s, \vec{\mathbf{x}}_r)$ obtained at frequency $\omega_0/2\pi = 3\text{MHz}$.

An alternative way of implementing the single scattering filter was proposed in [25] where the rotation and the rank one projection is performed in a more efficient way that does not disregard half of the array data as in [2, 3]. A more general filtering methodology that combines the LCT time-frequency selection procedure with a selection of the direction of arrival of the coherent echoes was recently proposed in [18]. In this approach the expected Hankel structure of the coherent scattered

field is also exploited. More specifically, the method in [18] defines the Hankel matrix that best approximates the data, and then uses plane wave decompositions of the result to detect the direction of arrival of the desired coherent echoes. The additional filtering in the direction of arrival improves the signal to noise ratio especially in the case of multiple reflectors located at the same distance from the array.

7.2 The single scattering filter

Let us re-write the single scattering filter [2, 3] in an equivalent and arguably simpler form. We divide the medium to be imaged in layers (slices) of thickness ΔL. For a given depth level L (center of a slice) we first time-window the data

$$P_T(t, \vec{\mathbf{x}}_s, \vec{\mathbf{x}}_r) = P(t, \vec{\mathbf{x}}_s, \vec{\mathbf{x}}_r)\phi(t - c_0 T) \tag{7.1}$$

where ϕ is a cut-off function with width $\Delta T = 2\Delta L/c_0$ and $T = 2L/c_0$. We set

$$P_T(\vec{\mathbf{x}}_s, \vec{\mathbf{x}}_r, t) = \frac{\sum_{\rho,\sigma} P_T\left(t + \frac{(\mathbf{x}_\rho - \mathbf{x}_\sigma)^2}{4c_0 L} - \frac{(\mathbf{x}_r - \mathbf{x}_s)^2}{4c_0 L}, \vec{\mathbf{x}}_\rho, \vec{\mathbf{x}}_\sigma\right)\psi_1(\mathbf{x}_\sigma, \mathbf{x}_\rho; \mathbf{x}_s, \mathbf{x}_r)}{\sum_{\rho,\sigma}\psi_1(\mathbf{x}_\sigma, \mathbf{x}_\rho; \mathbf{x}_s, \mathbf{x}_r)}$$

or, in frequency domain

$$\widehat{P}_T(\vec{\mathbf{x}}_s, \vec{\mathbf{x}}_r, \omega) = e^{i\frac{\omega}{4c_0 L}(\mathbf{x}_s - \mathbf{x}_r)^2}\frac{\sum_{\rho,\sigma}\widehat{P}_T(\mathbf{x}_s, \mathbf{x}_r, \omega)e^{-i\frac{\omega}{4c_0 L}(\mathbf{x}_\rho - \mathbf{x}_\sigma)^2}\psi_1(\mathbf{x}_\sigma, \mathbf{x}_\rho; \mathbf{x}_s, \mathbf{x}_r)}{\sum_{\rho,\sigma}\psi_1(\mathbf{x}_\sigma, \mathbf{x}_\rho; \mathbf{x}_s, \mathbf{x}_r)} \tag{7.2}$$

Here ψ_1 is a cut-off function which the authors at [3] take of the form

$$\psi_1(\mathbf{x}_\sigma, \mathbf{x}_\rho; \mathbf{x}_s, \mathbf{x}_r) = \delta(\mathbf{x}_\sigma + \mathbf{x}_\rho - \mathbf{x}_s - \mathbf{x}_r)$$

where δ is a Kronecker. With this choice of ψ_1 we have in the paraxial regime

$$P_T(\vec{\mathbf{x}}_s, \vec{\mathbf{x}}_r, t) = \frac{\sum_{\rho,\sigma} P_T\left(t + \frac{|\vec{\mathbf{x}}_\sigma - \vec{\mathbf{y}}^0| + |\vec{\mathbf{x}}_\rho - \vec{\mathbf{y}}^0| - |\vec{\mathbf{x}}_s - \vec{\mathbf{y}}^0| - |\vec{\mathbf{x}}_r - \vec{\mathbf{y}}^0|}{c_0}, \vec{\mathbf{x}}_\rho, \vec{\mathbf{x}}_\sigma\right)\psi_1(\mathbf{x}_\sigma, \mathbf{x}_\rho; \mathbf{x}_s, \mathbf{x}_r)}{\sum_{\rho,\sigma}\psi_1(\mathbf{x}_\sigma, \mathbf{x}_\rho; \mathbf{x}_s, \mathbf{x}_r)} \tag{7.3}$$

where $\vec{\mathbf{y}}^0 = (0, L)$.

Let us now briefly explain why this filter enhances the single scattering components of the data. The scattered field can be written as the sum of a single scattering contribution $\widehat{P}_T^S(\omega, \vec{\mathbf{x}}_s, \vec{\mathbf{x}}_r)$ and a multiple scattering contribution $\widehat{P}_T^M(\omega, \vec{\mathbf{x}}_s, \vec{\mathbf{x}}_r)$,

$$\widehat{P}_T(\omega, \vec{\mathbf{x}}_s, \vec{\mathbf{x}}_r) = \widehat{P}_T^S(\omega, \vec{\mathbf{x}}_s, \vec{\mathbf{x}}_r) + \widehat{P}_T^M(\omega, \vec{\mathbf{x}}_s, \vec{\mathbf{x}}_r),$$

where the single scattering contribution is of the form,

$$\widehat{P}_T^S(\omega, \vec{\mathbf{x}}_s, \vec{\mathbf{x}}_r) = \int_{\mathcal{I}_{\mathrm{W_L}}} \mathrm{d}\vec{\mathbf{y}}\ \rho(\vec{\mathbf{y}})\frac{1}{16\pi^2|\vec{\mathbf{y}} - \vec{\mathbf{x}}_s||\vec{\mathbf{y}} - \vec{\mathbf{x}}_r|}e^{i\frac{\omega}{c_0}(|\vec{\mathbf{y}} - \vec{\mathbf{x}}_s| + |\vec{\mathbf{y}} - \vec{\mathbf{x}}_r|)}$$

with $\mathcal{I}_{\mathrm{W_L}}$ the imaging window area corresponding to depth $[L - \Delta L/2, L + \Delta L/2]$. In the paraxial regime it reduces to

$$\widehat{P}_T^S(\omega, \vec{\mathbf{x}}_s, \vec{\mathbf{x}}_r) = e^{i\frac{\omega}{4c_0 L}(\mathbf{x}_s - \mathbf{x}_r)^2}\int_{\mathcal{I}_{\mathrm{W_L}}} \mathrm{d}\vec{\mathbf{y}}\ \rho(\vec{\mathbf{y}})\frac{1}{16\pi^2 L^2}e^{i\frac{\omega}{c_0}\left(2z + \frac{\left(\frac{\mathbf{x}_s + \mathbf{x}_s}{2} - \mathbf{y}\right)^2}{L}\right)} \tag{7.4}$$

where $\vec{\mathbf{y}} = (\mathbf{y}, z)$. We observe from (7.4) that the dependance on the difference variable $(\mathbf{x}_s - \mathbf{x}_r)$ of the single scattering contribution is known and is independent of the reflectivity. The filter (7.1)-(7.3) leaves the single scattering contribution (7.4) unchanged. Assuming that the multiple scattering contributions are random i.i.d with mean zero, they are reduced by the application of the filter by a factor of the order $\sqrt{N}$ with N the number of array elements assuming $N = N_s = N_r$.

7.3 Generalized windowed beamformer energy functional

We want now to generalize the windowed beamformer energy function so as to include the single scattering filter (or generalized formulations of it). For a search point $\vec{\mathbf{y}}^S$ we first filter the data as

$$\begin{aligned} P(\vec{\mathbf{x}}_s, \vec{\mathbf{x}}_r, t; \vec{\mathbf{y}}^S) &= \sum_{\sigma,\rho} \psi(\mathbf{x}_\sigma, \mathbf{x}_\rho; \mathbf{x}_s, \mathbf{x}_r) \\ &\times P\left(t + \frac{\left|\vec{\mathbf{x}}_\sigma - \vec{\mathbf{y}}^S\right| + \left|\vec{\mathbf{x}}_\rho - \vec{\mathbf{y}}^S\right| - \left|\vec{\mathbf{x}}_s - \vec{\mathbf{y}}^S\right| - \left|\vec{\mathbf{x}}_r - \vec{\mathbf{y}}^S\right|}{c_0}, \vec{\mathbf{x}}_\rho, \vec{\mathbf{x}}_\sigma\right) \end{aligned} \tag{7.5}$$

and we define

$$\mathcal{I}^{\mathbf{WBE}}(\vec{\mathbf{y}}^S) = \sum_{s,r} \int \mathrm{d}t \left| \phi\left(t - \frac{\left|\vec{\mathbf{x}}_s - \vec{\mathbf{y}}^S\right| - \left|\vec{\mathbf{x}}_r - \vec{\mathbf{y}}^S\right|}{c_0}\right) P(\vec{\mathbf{x}}_s, \vec{\mathbf{x}}_r, t; \vec{\mathbf{y}}^S) \right|^2 \tag{7.6}$$

We consider spatial cut-off functions of the form

$$\psi(\mathbf{x}_\sigma, \mathbf{x}_\rho; \mathbf{x}_s, \mathbf{x}_r) = \psi_0(\mathbf{x}_\rho - \mathbf{x}_r)\psi_0(\mathbf{x}_\sigma - \mathbf{x}_s)\psi_1(\mathbf{x}_\sigma + \mathbf{x}_\rho - \mathbf{x}_s - \mathbf{x}_r) \tag{7.7}$$

with even functions ψ_0, ψ_1. Note that one can use P_T instead of the traces in (7.5) where P_T is defined as in (7.1) with L being the depth of $\vec{\mathbf{y}}^S$. Therefore the filter (7.5) is similar to (7.3). Remark also that (7.6) is a generalization of the windowed beamformer energy functional (6.4) and reduces to it for $\psi_1 = 1$, $\psi_0 = \psi_{\mathcal{X}}$ and $\phi = \phi_{\mathcal{T}}$.

The filter's implementation

Here we want to explain the implementation of the generalized windowed beamformer energy function (7.6). To do so, we change adequately the algorithm described in Section 6.3. The only step that is modified is the 4^{th} step in which $\tilde{Q}_{\mathcal{T}}$ is defined now as:

$$\tilde{Q}_{\mathcal{T}}(\omega, k_r, k_s; \vec{\mathbf{y}}^S) = \widehat{Q}_{\mathcal{T}}(\omega, k_r, k_s; \vec{\mathbf{y}}^S)\widehat{\Psi}(k_s, k_r) \tag{7.8}$$

with $\widehat{\Psi}(k_s, k_r)$ of the form

$$\widehat{\Psi}(k_s, k_r) = \widehat{\psi}(k_s)\widehat{\psi}(k_r)\widehat{\xi}(k_s + k_r) \tag{7.9}$$

with

$$\widehat{\psi}(k_s) = \exp\left(-k_s^2 \frac{\beta^2}{2}\right) \tag{7.10}$$

and $\widehat{\xi}$ defined as

$$\widehat{\xi}(k_s + k_r) = \exp\left(\frac{\beta^2(k_s + k_r)^2}{2(2 - \alpha^2/\beta^2)}\right). \tag{7.11}$$

In our numerics we consider α to be non-zero but small and $\beta = \mathcal{X}(\omega_0) = \mathcal{X}$.

For $\alpha = 0$ we recover the single scattering filter and $\widehat{\Psi}$ becomes

$$\begin{aligned}
\widehat{\Psi}(k_s, k_r) &= \sqrt{\frac{\pi}{\beta^2}} \exp\left(-k_s^2 \frac{\beta^2}{2}\right) \exp\left(-k_r^2 \frac{\beta^2}{2}\right) \exp\left(\beta^2 \frac{(k_s + k_r)^2}{4}\right) \\
&= \sqrt{\frac{\pi}{\beta^2}} \exp\left(-k_s^2 \frac{\beta^2}{4}\right) \exp\left(-k_r^2 \frac{\beta^2}{4}\right) \exp\left(\frac{\beta^2}{2} k_s k_r\right) \\
&= \sqrt{\frac{\pi}{\beta^2}} \exp\left(-\beta^2 \frac{(k_s - k_r)^2}{4}\right)
\end{aligned} \tag{7.12}$$

For $\alpha \neq 0$ the expression for $\widehat{\Psi}$ is

$$\widehat{\Psi}(k_s, k_r) = \sqrt{\frac{\pi}{\beta^2 - 2\alpha^2}} \exp\left(-k_r^2 \frac{\beta^4 - \alpha^2\beta^2}{4\beta^2 - 2\alpha^2}\right) \exp\left(-k_s^2 \frac{\beta^4 - \alpha^2\beta^2}{4\beta^2 - 2\alpha^2}\right) \exp\left(k_r k_s \frac{\beta^4}{2\beta^2 - \alpha^2}\right). \tag{7.13}$$

The derivation of the expressions (7.12) and (7.13) is carried out in the Appendix A.

7.4 Numerical results

To test the effect of the filter we try to image objects embedded in stronger clutter. To do so we increase the standard deviation of the fluctuations to $\sigma = 4\%$ instead of $\sigma = 3\%$ we used in the previous realizations of the background medium.

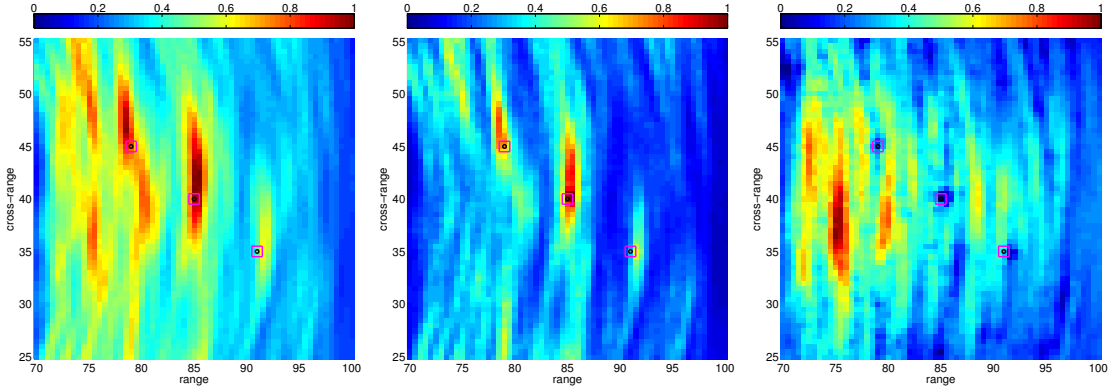

(a) *WBE image.* **(b)** *WBE image with filter.* **(c)** *The filter's effect.*

Figure 7.2: Windowed beamformer energy images and the single scattering filter.

We illustrate in Figure 7.3 the results obtained for another realization of the background medium with the same statistical characteristics as in Figure 7.2.

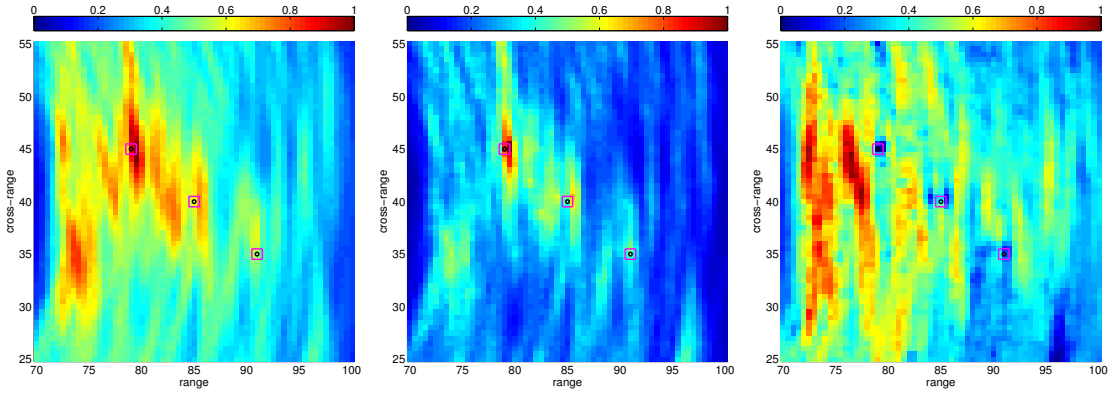

(a) *WBE image* **(b)** *WBE image with filter.* **(c)** *The filter's effect.*

Figure 7.3: Windowed beamformer energy images and the single scattering filter.

The images shown on the left column in figures 7.2 and 7.3 are obtained using the $\mathcal{I}^{\mathbf{WBE}}$ imaging functional as defined in (6.11) while the images in the middle column (WBE with filter) are obtained with the same functional but using the modified $\tilde{Q}_{\mathcal{T}}$ defined by (7.8) and $\widehat{\Psi}$ given by (7.13) with $\alpha = \beta\sqrt{2+10^{-5}}$, $\beta = \mathcal{X} = 2\text{mm}$ and $\mathcal{T} = 1.05848\mu\text{sec}$. As we can see, in both figures, the images we obtain using the windowed beamformer energy imagining functional (left image) are too noisy, and we cannot distinguish the scatterers from the background's medium inhomogeneities. By applying the single scattering filter we observe a significant improvement in the signal to noisy ratio as the spurious peaks associated with the background's medium inhomogeneities are dramatically reduced. In Figure 7.2c and Figure 7.3c the effect of the single scattering filter on the image is shown by plotting the difference of the image obtained with WBE and the one obtained using WBE with the single scattering filter. The image is normalized by its maximal value. We can clearly see that the filter applied to the data leaves the single scattering components unchanged as we remark by looking at the targets' area where the effect of the filter is almost zero. The filter, however averages out the multiple scattering components of the data. These results suggest that looking at the zeros of the difference between the two images with and without the filter may be a good way to detect the presence of coherent scatters.

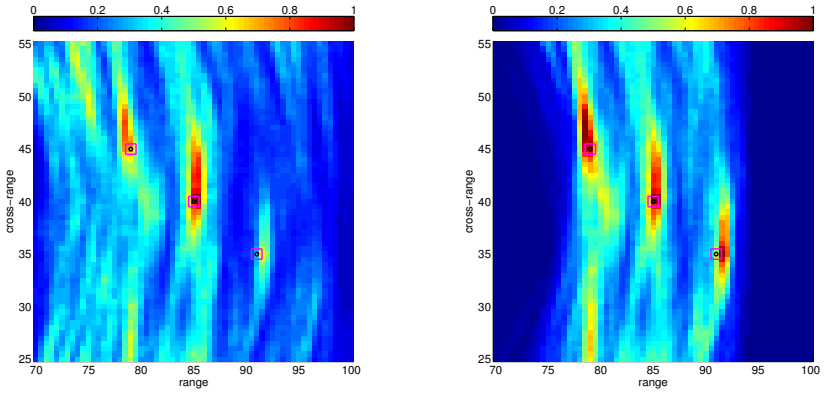

(a) *WBE image with filter.* **(b)** *RWBE image with filter.*

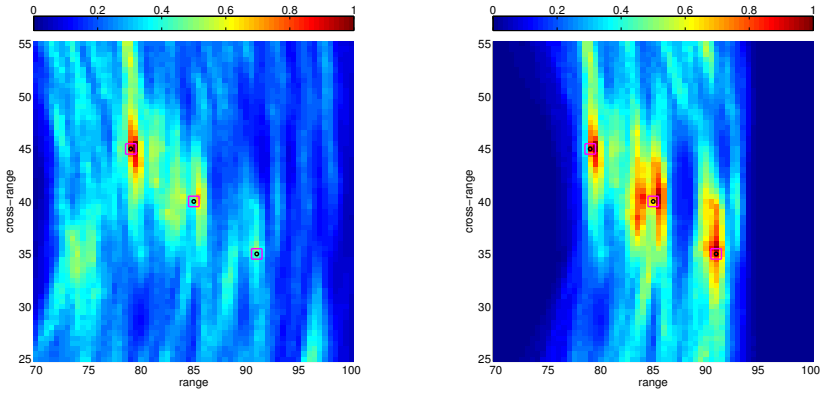

(c) *WBE image with filter.* **(d)** *RWBE image with filter.*

Figure 7.4: Windowed beam-forming $\mathcal{I}^{\mathbf{WBE}}$ and refined windowed beam-forming $\mathcal{I}^{\mathbf{RWBE}}$ images for two different realizations of the background medium with the same statistical characteristics.

Since we can locate the reflectors using the single scattering filter, the idea is to make the filter more efficient by taking appropriate windows in time. We use a function $\phi_{\mathcal{R}}$ to window the data time traces. The function $\phi_{\mathcal{R}}$ is the indicator function:

$$\phi_{\mathcal{R}}(t) = 1_{[T'-\Delta T'/2,\, T'+\Delta T'/2]}(t)$$

where $T' = 2L'/c_0$ is the appropriate time for a given depth level L' and $\Delta T' = 2\Delta L'/c_0$ is the size of the window in time in order to get a window in the range direction of the size $\Delta L'$. Instead of working with the traces $P(\vec{\mathbf{x}}_s, \vec{\mathbf{x}}_r, t)$ we use the windowed data and set $P(\vec{\mathbf{x}}_s, \vec{\mathbf{x}}_r, t) = \phi_{\mathcal{R}}(t)P(\vec{\mathbf{x}}_s, \vec{\mathbf{x}}_r, t)$ for every given depth level L' and $\Delta T'$. We define the refined imaging function $\mathcal{I}^{\mathbf{RWBE}}$ as the sum of the WBE images we obtain for every L' and $\Delta T'$. Using this approach we obtained Figure 7.4b and Figure 7.4d. Here we used three windows with a duration of $\Delta T' = 2.8296\mu$sec each and centered to the range of the targets which we assume that can be estimated approximately from the initial $\mathcal{I}^{\mathbf{WBE}}$ image. We remark that the refined WBE image allows us to improve the SNR for the scatterers that are further away from the array.

Until now the best images we obtained for the two realizations of the heavy cluttered media are illustrated in Figure 7.4b and Figure 7.4d but they do not have good resolution in cross-range. This is done in purpose. In a first step we need to create images using a small value for $\mathcal{X}$. The images will be stable but blurry

in the cross-range direction. We do not worry about cross-range resolution in this first step, we need however to localize the targets in range. After the localization in range we first refine the resolution with the $\mathcal{I}^{\mathbf{RWBE}}$. We can then further improve the image by adjusting the smoothing parameters so as to determine the optimal ones. The final images for the two different realizations of the heavy cluttered media using the optimal smoothing parameters are shown in Figure 7.5.

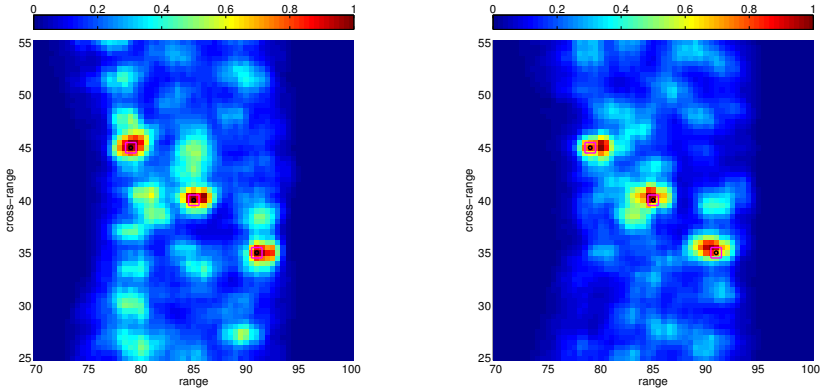

(a) *Final WBE image.* **(b)** *Final WBE image.*

Figure 7.5: Refined windowed beamformer energy $\mathcal{I}^{\mathbf{RWBE}}$ images obtained using the optimal smoothing parameters for two different realizations of the background medium with the same statistical characteristics.

The optimal smoothing parameters we used to form the images in Figure7.5 are $\mathcal{T} = 3.15448\mu$sec for smoothing in the range direction and $\mathcal{X} = 10$mm for smoothing in the cross-range direction.

Comparing now the Figure7.2a and the Figure7.3a with the correspondingly Figure7.5a and Figure7.5b, one can observe a significant improvement. The role of the single scattering filter as it was introduced in the imaging function $\mathcal{I}^{\mathbf{WBE}}$, as well as the refined $\mathcal{I}^{\mathbf{RWBE}}$ imaging and the optimization over the smoothing parameters were crucial in the obtention of stable images with high resolution in multiple scattering media.

8 Summary and conclusions

We considered here the problem of imaging reflectors embedded in inhomogeneous media with random fluctuations in the wave speed. The reflectors that we are seeking for are also an inhomogeneity in the medium. We assume that the background medium fluctuations are not known and cannot be estimated. Therefore we model them as a random process. Our data is the array response matrix that can be obtained by sending sequentially from each array element a short pulse and then record the scattered echoes at all array elements. The waves propagate in the background medium and interact with the medium inhomogeneities before and after being scattered by the reflectors that we wish to image. Therefore the imaging problem is very challenging. To image we use a statistically stable imaging functional called the windowed beamformer energy (WBE) functional. Statistical stability here means that the imaging results do not depend on the particular realization of the random medium fluctuations considered. The statistical stability of WBE follows from the statistical stability of coherent interferometric (CINT) imaging functional since WBE was shown to be equivalent to CINT. Compared to CINT, the WBE functional is easier to implement both in software and in hardware. Moreover, for typical values of the imaging parameters in medical ultrasound or the non-destructive testing regime, creating an image with WBE is significantly faster than with CINT. In our examples WBE was 5 to 10 times faster than CINT. To increase the efficiency and robustness of the WBE functional we also incorporated a filter that aims to enhancing the single scattering component of the recorded echoes. This means that artefacts due to the multiple scattering of the waves with the medium inhomogeneities are significantly reduced with the application of the filter. We show with numerical simulations carried out in ultrasound medical imaging regime that the proposed filter dramatically improves the signal to noise ratio of the image.

Appendices

A The filter

We want to generalize the implementation algorithm for the $\mathcal{I}^{\mathbf{WBE}}$ imaging functional so as to include a spatial cut-off function of the form

$$\psi(\mathbf{x}_\rho, \mathbf{x}_\sigma; \mathbf{x}_r, \mathbf{x}_s) = \psi_0(\mathbf{x}_\rho - \mathbf{x}_r)\psi_0(\mathbf{x}_\sigma - \mathbf{x}_s)\psi_1(\mathbf{x}_\rho + \mathbf{x}_\sigma - \mathbf{x}_r - \mathbf{x}_s) \tag{A.1}$$

For that let us define in the Fourier domain a function

$$\widehat{\Psi}(k_s, k_r) = \widehat{\psi}(k_s)\widehat{\psi}(k_r)\widehat{\xi}(k_s + k_r) \tag{A.2}$$

with $\widehat{\psi}$ a Gaussian,

$$\widehat{\psi}(k_s) = \exp\left(-k_s^2\frac{\beta^2}{2}\right) \tag{A.3}$$

and the function $\widehat{\xi}$ defined by

$$\widehat{\xi}(k_s + k_r) = \exp\left(\frac{\beta^2(k_s + k_r)^2}{2(2 - \alpha^2/\beta^2)}\right) \tag{A.4}$$

and we consider a small and $\beta = \mathcal{X}(\omega_0) = \mathcal{X}$.

Let us consider the following convolution integral

$$\mathcal{I} = \int \mathrm{d}x_\rho \int \mathrm{d}x_\sigma\ u(\mathbf{x}_\rho, \mathbf{x}_\sigma; t)\psi_0(\mathbf{x}_r - \mathbf{x}_\rho)\psi_0(\mathbf{x}_s - \mathbf{x}_\sigma)\psi_1(\mathbf{x}_r + \mathbf{x}_s - \mathbf{x}_\rho - \mathbf{x}_\sigma) \tag{A.5}$$

that appears in the $\mathcal{I}^{\mathbf{WBE}}$ functional. By replacing in (A.5) u, ψ_0 and ψ_1 by their Fourier transforms we obtain

$$\begin{aligned}\mathcal{I} \ = & \int \mathrm{d}x_\rho \int \mathrm{d}x_\sigma \int \mathrm{d}\omega_\rho \int \mathrm{d}\omega_\sigma\ \widehat{u}(\omega_\rho, \omega_\sigma)e^{i(\omega_\rho\mathbf{x}_\rho + \omega_\sigma\mathbf{x}_\sigma)} \\ & \times \int \mathrm{d}k_r\ \widehat{\psi}_0\psi_0(k_r)e^{ik_r(\mathbf{x}_r - \mathbf{x}_\rho)} \int \mathrm{d}k_s\ \widehat{\psi}_0(k_s)e^{ik_s(\mathbf{x}_s - \mathbf{x}_\sigma)} \\ & \times \int \mathrm{d}\delta\ \widehat{\psi}_1(\delta)e^{i\delta(\mathbf{x}_r + \mathbf{x}_s - \mathbf{x}_\rho - \mathbf{x}_\sigma)}\end{aligned}$$

which can be re-written as

$$\begin{aligned}\mathcal{I} = & \int \mathrm{d}\omega_\rho \int \mathrm{d}\omega_\sigma \int \mathrm{d}k_r \int \mathrm{d}k_s \int \mathrm{d}\delta\ \widehat{u}(\omega_\rho, \omega_\sigma)\widehat{\psi}_0(k_r)\widehat{\psi}_0(k_s)\widehat{\psi}_1(\delta) \\ & \times e^{i(k_r\mathbf{x}_r + k_s\mathbf{x}_s + \delta\mathbf{x}_r + \delta\mathbf{x}_s)} \int \mathrm{d}x_\rho\ \ e^{i\mathbf{x}_\rho(\omega_\rho - k_r - \delta)} \int \mathrm{d}x_\sigma\ \ e^{i\mathbf{x}_\sigma(\omega_\sigma - k_s - \delta)}.\end{aligned}$$

From the last two Fourier integrals we get the delta functions $\delta(\omega_\rho - k_r - \delta)$ and $\delta(\omega_\sigma - k_s - \delta)$, so that $\omega_\rho = k_r + \delta$ and $\omega_\sigma = k_s + \delta$ and $\mathcal{I}$ reduces to

$$\mathcal{I} = \int \mathrm{d}k_r \int \mathrm{d}k_s \int \mathrm{d}\delta\ \widehat{u}(k_r + \delta, k_s + \delta)\widehat{\psi}_0(k_r)\widehat{\psi}_0(k_s)\widehat{\psi}_1(\delta)e^{i(k_r\mathbf{x}_r + k_s\mathbf{x}_s + \delta\mathbf{x}_r + \delta\mathbf{x}_s)} \tag{A.6}$$

For the single scattering filter we have

$$\psi_1(\mathbf{x}_r + \mathbf{x}_s - \mathbf{x}_\rho - \mathbf{x}_\sigma) = \delta(\mathbf{x}_r + \mathbf{x}_s - \mathbf{x}_\rho - \mathbf{x}_\sigma) \tag{A.7}$$

and therefore in this case $\widehat{\psi}_1 = 1$. So (A.6) becomes

$$\begin{aligned}\mathcal{I} &= \int \mathrm{d}k_r \int \mathrm{d}k_s \int \mathrm{d}\delta\ \widehat{u}(k_r+\delta, k_s+\delta)\widehat{\psi}_0(k_r)\widehat{\psi}_0(k_s) \\ &\qquad \times \exp\left(i\left[(k_r+\delta)\mathbf{x}_r + (k_s+\delta)\mathbf{x}_s\right]\right) \\ &= \int \mathrm{d}\widetilde{k}_r \int \mathrm{d}\widetilde{k}_s \widehat{u}(\widetilde{k}_r, \widetilde{k}_s) \exp\left(i(\widetilde{k}_r\mathbf{x}_r + \widetilde{k}_s\mathbf{x}_s)\right) \\ &\qquad \times \int \mathrm{d}\delta\ \widehat{\psi}_0(\widetilde{k}_r - \delta)\widehat{\psi}_0(\widetilde{k}_s - \delta) \end{aligned} \tag{A.8}$$

with $\widetilde{k}_r = k_r - \delta$ and $\widetilde{k}_s = k_s - \delta$. This means that we can implement the filter by replacing in the 4^{th} step of the algorithm $\widehat{\psi}_0(k_r)\widehat{\psi}_0(k_s)$ by

$$\widetilde{\psi}(k_r, k_s) = \int \mathrm{d}\delta\ \widehat{\psi}_0(k_r - \delta)\widehat{\psi}_0(k_s - \delta) \tag{A.9}$$

which for the Gaussian $\widehat{\psi}_0$ defined in (A.3) becomes

$$\begin{aligned}\widetilde{\psi}(k_r, k_s) &= \int_{-\infty}^{+\infty} \widehat{\psi}_0(k_r - \delta)\widehat{\psi}_0(k_s - \delta)\ \mathrm{d}\delta \\ &= \int_{-\infty}^{+\infty} \mathrm{d}\delta\ \exp\left(-\frac{\beta^2(k_r-\delta)^2}{2} - \frac{\beta^2(k_s-\delta)^2}{2}\right) \\ &= \exp\left(-\frac{\beta^2 k_r^2}{2} - \frac{\beta^2 k_s^2}{2}\right) \int_{-\infty}^{+\infty} \mathrm{d}\delta\ \exp\left(-\beta^2\left(\delta^2 - \delta(k_r+k_s)\right)\right) \\ &= \exp\left(-\frac{\beta^2 k_r^2}{2} - \frac{\beta^2 k_s^2}{2}\right) \exp\left(\frac{\beta^2(k_r+k_s)^2}{4}\right) \frac{\sqrt{\pi}}{\beta} \\ &= \frac{\sqrt{\pi}}{\beta} \exp\left(-\frac{\beta^2 k_r^2}{2} - \frac{\beta^2 k_s^2}{2}\right) \exp\left(\frac{\beta^2(k_r+k_s)^2}{4}\right) \\ &= \frac{\sqrt{\pi}}{\beta} \exp\left(-\frac{\beta^2(k_r-k_s)^2}{4}\right) \end{aligned} \tag{A.10}$$

In our numerical simulations we have considered a more general function ψ_1 instead of (A.7). Specifically, we take a Gaussian function that decays away from the diagonal. In this case the Fourier transform of ψ_1 is of the form

$$\widehat{\psi}_1(\delta) = \exp\left(-\frac{\alpha^2\delta^2}{2}\right) \tag{A.11}$$

with α small. Note that for $\alpha = 0$ we recover the function (A.7). For a Gaussian $\widehat{\psi}_1$ as in (A.11), (A.8) becomes

$$\begin{aligned}\mathcal{I} = &\int \mathrm{d}k_r \int \mathrm{d}k_s \int \mathrm{d}\delta\ \widehat{u}(k_r+\delta, k_s+\delta)\widehat{\psi}_0(k_r)\widehat{\psi}_0(k_s) \\ &\times \exp\left(i\left[(k_r+\delta)\mathbf{x}_r + (k_s+\delta)\mathbf{x}_s\right]\right) \exp\left(-\frac{\alpha^2\delta^2}{2}\right) \\ &= \int \mathrm{d}\widetilde{k}_r \int \mathrm{d}\widetilde{k}_s\ \widehat{u}(\widetilde{k}_r, \widetilde{k}_s) \exp\left(i(\widetilde{k}_r\mathbf{x}_r + \widetilde{k}_s\mathbf{x}_s)\right) \\ &\times \int \mathrm{d}\delta\ \widehat{\psi}_0(\widetilde{k}_r - \delta)\widehat{\psi}_0(\widetilde{k}_s - \delta) \exp\left(-\frac{\alpha^2\delta^2}{2}\right) \end{aligned} \tag{A.12}$$

This means that we can implement the filter by replacing in the 4^{th} step of the algorithm $\widehat{\psi}_0(k_r)\widehat{\psi}_0(k_s)$ by

$$\widetilde{\psi}(k_r,k_s) = \int \mathrm{d}\delta\ \widehat{\psi}_0(k_r-\delta)\widehat{\psi}_0(k_s-\delta)\exp\left(-\frac{\alpha^2\delta^2}{2}\right) \tag{A.13}$$

which for the Gaussian $\widehat{\psi}_0$ defined in (A.3) becomes

$$\begin{aligned}
\widetilde{\psi}(k_r,k_s) = &\int_{-\infty}^{+\infty} \mathrm{d}\delta\ \exp\left(-\frac{\beta^2}{2}\left(k_r^2+k_s^2-2\delta(k_r+k_s)+\delta^2(2-\frac{\alpha^2}{\beta^2})\right)\right)\\
= &\sqrt{\frac{\pi}{\beta^2-2\alpha^2}}\exp\left(-\frac{\beta^2k_r^2}{2}-\frac{\beta^2k_s^2}{2}\right)\exp\left(\frac{\beta^2(k_r+k_s)^2}{2\left(2-\frac{\alpha^2}{\beta^2}\right)}\right)\\
= &\sqrt{\frac{\pi}{\beta^2-2\alpha^2}}\exp\left(-\frac{\beta^2}{2}\frac{1-\eta}{2-\eta}k_r^2-\frac{\beta^2}{2}\frac{1-\eta}{2-\eta}k_s^2+\frac{\beta^2}{2}\frac{2}{2-\eta}k_rk_s\right)
\end{aligned} \tag{A.14}$$

with $\eta=\frac{\alpha^2}{\beta^2}$. In the numerics we take $\eta=2+\epsilon$ with $\epsilon>0$ small.

References

[1] Ricardo Alonso, Liliana Borcea, George Papanicolaou, and Chrysoula Tsogka. Detection and imaging in strongly backscattering randomly layered media. *Inverse Problems*, 27(2):025004, 2011. 30

[2] Alexandre Aubry and Arnaud Derode. Detection and imaging in a random medium: A matrix method to overcome multiple scattering and aberration. *Journal of Applied Physics*, 106(4):044903, 2009. 3, 30, 31, 32

[3] Alexandre Aubry and Arnaud Derode. Random matrix theory applied to acoustic backscattering and imaging in complex media. *Physical review letters*, 102(8):084301, 2009. 3, 12, 30, 31, 32

[4] Éliane Bécache, Patrick Joly, and Chrysoula Tsogka. Etude d'un nouvel élément fini mixte permettant la condensation de masse. *Comptes Rendus de l'Académie des Sciences-Series I-Mathematics*, 324(11):1281–1286, 1997. 13

[5] Eliane Bécache, Patrick Joly, and Chrysoula Tsogka. An analysis of new mixed finite elements for the approximation of wave propagation problems. *SIAM Journal on Numerical Analysis*, 37(4):1053–1084, 2000. 13

[6] Jean-Pierre Berenger. A perfectly matched layer for the absorption of electromagnetic waves. *Journal of computational physics*, 114(2):185–200, 1994. 13

[7] N Bleistein, JK Cohen, and JW Stockwell. *Mathematics of multidimensional seismic imaging, migration, and inversion*. Springer, 2001. 1

[8] Liliana Borcea, F Gonzalez Del Cueto, George Papanicolaou, and Chrysoula Tsogka. Filtering random layering effects in imaging. *Multiscale Modeling & Simulation*, 8(3):751–781, 2010. 30

[9] Liliana Borcea, Josselin Garnier, George Papanicolaou, and Chrysoula Tsogka. Coherent interferometric imaging, time gating and beamforming. *Inverse Problems*, 27(6):065008, 2011. 1, 3

[10] Liliana Borcea, Josselin Garnier, George Papanicolaou, and Chrysoula Tsogka. Enhanced statistical stability in coherent interferometric imaging. *Inverse problems*, 27(8):085004, 2011. 1, 3

[11] Liliana Borcea, George Papanicolaou, and Chrysoula Tsogka. A resolution study for imaging and time reversal in. In *Inverse Problems: Theory and Applications: INdAM Workshop on Inverse Problems and Applications, June 3-9, 2002, Cortona, Italy: Special Session at AMS-UMI First Joint International Meeting on Inverse Boundary Problems and Applications, June 12-16, 2002, Pisa, Italy*, volume 333, page 63. American Mathematical Soc., 2003. 17

[12] Liliana Borcea, George Papanicolaou, and Chrysoula Tsogka. Theory and applications of time reversal and interferometric imaging. *Inverse Problems*, 19(6):S139, 2003. 17

[13] Liliana Borcea, George Papanicolaou, and Chrysoula Tsogka. Interferometric array imaging in clutter. *Inverse Problems*, 21(4):1419, 2005. 1

[14] Liliana Borcea, George Papanicolaou, and Chrysoula Tsogka. Adaptive interferometric imaging in clutter and optimal illumination. *Inverse Problems*, 22(4):1405, 2006. 1, 18, 25

[15] Liliana Borcea, George Papanicolaou, and Chrysoula Tsogka. Coherent interferometric imaging in clutter: Geopysics, 71. *SI165–SI175*, 313, 2006.

[16] Liliana Borcea, George Papanicolaou, and Chrysoula Tsogka. Asymptotics for the space-time wigner transform with applications to imaging. *Stochastic Differential Equations: Theory and Applications (in Honor of Prof. Boris L. Rozovskii), Interdiscip. Math. Sci*, 2:91–112, 2007. 25

[17] Liliana Borcea, George Papanicolaou, and Chrysoula Tsogka. Adaptive time-frequency detection and filtering for imaging in heavy clutter. *SIAM Journal on Imaging Sciences*, 4(3):827–849, 2011. 30

[18] Liliana Borcea, George Papanicolaou, and Chrysoula Tsogka. Adaptive time-frequency detection and filtering for imaging in heavy clutter. *Waves in random and complex media*, 2016. submitted. 31, 32

[19] Liliana Borcea, George Papanicolaou, and Chrysoula Tsogka. Time and direction of arrival detection and filtering for imaging in strongly scattering random media. *arXiv preprint arXiv:1603.05223*, 2016.

[20] M Klemm, IJ Craddock, JA Leendertz, A Preece, and R Benjamin. Improved delay-and-sum beamforming algorithm for breast cancer detection. *International Journal of Antennas and Propagation*, 2008, 2008. 21

[21] Claire Prada, Sebastien Manneville, Dimitri Spoliansky, and Mathias Fink. Decomposition of the time reversal operator: Detection and selective focusing on two scatterers. *J. Acoust. Soc. Am.*, 99:2067–2076, 1996. 31

[22] Sharfine Shahjahan, Alexandre Aubry, Fabienne Rupin, Bertrand Chassignole, and Arnaud Derode. A random matrix approach to detect defects in a strongly scattering polycrystal: How the memory effect can help overcome multiple scattering. *Applied Physics Letters*, 104(23):234105, 2014.

[23] Christiaan Cornelis Stolk. On the modeling and inversion of seismic data. 2001. 9

[24] Kai E Thomenius. Evolution of ultrasound beamformers. In *Ultrasonics Symposium, 1996. Proceedings., 1996 IEEE*, volume 2, pages 1615–1622. IEEE, 1996. 21

[25] Chrysoula Tsogka and Michalis Apostolopoulos. A comparative study of data filtering methods for imaging in strongly scattering media. *Wave Motion*, 68:97–113, 2017. 31